CHALMERS

Retrieval of ocean surface currents and winds using satellite SAR backscatter and Doppler frequency shift

ANIS ELYOUNCHA

Department of Space, Earth and Environment
CHALMERS UNIVERSITY OF TECHNOLOGY
Göteborg, Sweden 2020

THESIS FOR THE DEGREE OF DOCTOR OF PHILOSOPHY

Retrieval of ocean surface currents and winds using satellite SAR backscatter and Doppler frequency shift

ANIS ELYOUNCHA

Department of Space, Earth and Environment
Division of Microwave and Optical Remote Sensing
CHALMERS UNIVERSITY OF TECHNOLOGY

Göteborg, Sweden 2020

Retrieval of ocean surface currents and winds using satellite SAR backscatter and Doppler frequency shift
ANIS ELYOUNCHA
ISBN 978-91-7905-390-1

Doktorsavhandlingar vid Chalmers tekniska högskola
Ny serie nr 4857
ISSN 0346-718X

Department of Space, Earth and Environment
Division of Microwave and Optical Remote Sensing
Chalmers University of Technology
SE-412 96 Göteborg
Sweden
Telephone: +46 (0)31-772 5652

Cover:
The Öresund strait imaged by TanDEM-X. Copyright DLR 2014.

Chalmers digitaltryck
Göteborg, Sweden 2020

Retrieval of ocean surface currents and winds using satellite SAR backscatter and Doppler frequency shift
Thesis for the degree of Doctor of Philosophy
ANIS ELYOUNCHA
Department of Space, Earth and Environment
Division of Microwave and Optical Remote Sensing
Chalmers University of Technology

ABSTRACT

Ocean surface winds and currents play an important role for weather, climate, marine life, ship navigation, oil spill drift and search and rescue. In-situ observations of the ocean are sparse and costly. Satellites provide a useful complement to these observations. Synthetic aperture radar (SAR) is particularly attractive due to its high spatial resolution and its capability to extract both sea surface winds and currents day and night and almost independent of weather.

The work in this thesis involves processing of along-track interferometric SAR (ATI-SAR) data, analysis of the backscatter and Doppler frequency shift, and development of wind and current retrieval algorithms. Analysis of the Doppler frequency shift showed a systematic bias. A calibration method was proposed and implemented to correct for this bias. Doppler analysis also showed that the wave contribution to the SAR Doppler centroid often dominates over the current contribution. This wave contribution is estimated using existing theoretical and empirical Doppler models. For wind and current retrieval, two methods were developed and implemented.

The first method, called the direct method, consists of retrieval of the wind speed from SAR backscatter using an empirical backscatter model. In order to retrieve the radial current, the retrieved wind speed is used to correct for the wave contribution. The current retrieval was assessed using two different (theoretical and empirical) Doppler models and wind inputs (model and SAR-derived). It was found that the results obtained by combining the Doppler empirical model with the SAR-derived wind speed were more consistent with ocean models.

The second method, called Bayesian method, consists of blending the SAR observables (backscatter and Doppler shift) with an atmospheric and an oceanic model to retrieve the total wind and current vector fields. It was shown that this method yields more accurate estimates, i.e. reduces the models biases against in-situ measurements. Moreover, the method introduces small scale features, e.g. fronts and meandering, which are weakly resolved by the models.

The correlation between the surface wind vectors and the SAR Doppler shift was demonstrated empirically using the Doppler shift estimated from over 300 TanDEM-X interferograms and ECMWF reanalysis wind vectors. Analysis of polarimetric data showed that theoretical models such as Bragg and composite surface models over-estimate the backscatter polarization ratio and Doppler shift polarization difference. A combination of a theoretical Doppler model and an empirical modulation transfer function was proposed. It was found that this model is more consistent with the analyzed data than the pure theoretical models.

The results of this thesis will be useful for integrating SAR retrievals in ocean current products and assimilating SAR observables in the atmospheric, oceanic or coupled models. The results are also relevant for preparation studies of future satellite missions.

Keywords: Ocean surface currents, ocean surface winds, along-track InSAR, Doppler centroid analysis, synthetic aperture radar, Bayesian inversion.

ACKNOWLEDGEMENTS

First, I would like to express my sincere gratitude to my main supervisor Dr. Leif Eriksson, for giving me the opportunity to undertake this work, for the guidance, support and encouragement he has provided throughout the past 5 years. I would also like to specially thank my co-supervisor and examiner Prof. Lars Ulander, for the guidance, the fruitful discussions, the valuable advice and relevant inputs to my work. I am also grateful to Prof. Göran Broström and Prof. Roland Romeiser for their constructive feedback, valuable discussions and contributions to my papers. I would like to thank all my colleagues in the Department of Space, Earth and Environment for all kind of help, support and encouragement. Finally, I am so thankful to my family: my wife, my mother, my sister and my brother for their continued and unconditional support.

APPENDED PUBLICATIONS

This thesis is based on the work in the following appended publications:

- **A**. A. Elyouncha, L. E. B. Eriksson, R. Romeiser and L. M. H. Ulander, ”Measurements of Sea Surface Currents in the Baltic Sea Region Using Spaceborne Along-Track InSAR,” *IEEE Transactions on Geoscience and Remote Sensing, vol. 57, no. 11, pp. 8584-8599, Nov. 2019.*

- **B**. A. Elyouncha, L. E. B. Eriksson, R. Romeiser and L. M. H. Ulander, ”Empirical Relationship between the Doppler Centroid derived from X-Band Spaceborne InSAR Data and Wind Vectors,”. Manuscript submitted to *IEEE Transactions on Geoscience and Remote Sensing.*

- **C**. A. Elyouncha, L. E. B. Eriksson, G. Broström, L. Axell and L. M. H. Ulander, ”Joint Retrieval of Ocean Surface Wind and Current Vectors from Satellite SAR Data using a Bayesian Inversion Method,”. Manuscript submitted to *Remote Sensing of Environment.*

- **D**. A. Elyouncha, L. E. B. Eriksson, R. Romeiser and L. M. H. Ulander, ”Wind Direction Ambiguity Removal using Along-Track INSAR: A Case Study,”. *IEEE International Geoscience and Remote Sensing Symposium (IGARSS), Valencia, Spain, 22-27 July 2018.*

- **E**. A. Elyouncha, L. E. B. Eriksson, R. Romeiser and L. M. H. Ulander, ”Using Sentinel-1 Ocean Data for Mapping Sea Surface Currents Along the Southern Norwegian Coast,”. *IEEE International Geoscience and Remote Sensing Symposium (IGARSS), Yokohama, Japan, July 28 - August 2, 2019.*

RELATED PAPERS

The author has contributed to the following papers that are related to the work in this thesis, but are not appended in this thesis:

I. A. Elyouncha, L. E. B. Eriksson, R. Romeiser, G. K. Carvajal and L. M. H. Ulander, ”Wind-wave Effect on ATI-SAR Measurements of Ocean Surface Currents in the Baltic Sea,” *Proceedings of IEEE International Geoscience and Remote Sensing Symposium (IGARSS), Beijing, China, 10-15 July 2016, pp. 3982-3985.*

II. A. Elyouncha, L. E. B. Eriksson, R. Romeiser and L. M. H. Ulander, ”Phase Calibration of TanDEM-X ATI-SAR Data for Sea Surface Velocity Measurements,” *Proceedings of IEEE International Geoscience and Remote Sensing Symposium (IGARSS), Fort Worth, TX, USA, 23-28 July 2017, pp. 922-925.*

CONTENTS

Introduction 1

1.1 Motivation

The ocean plays a key role in the weather and climate through storage and transportation of energy and mass. The atmosphere and the ocean are coupled through surface fluxes (momentum, heat, water and gases). Despite being vital forcing fields for both atmospheric and oceanic models and essential in understanding the role of the ocean in the climate, these fluxes are poorly quantified. Numerical models are good tools to simulate the air-sea exchange and its effect on the climate. These models require surface boundary conditions and thus exhibit sensitivity to air-sea fluxes. The air-sea exchange is controlled by thermodynamical factors such as temperature and difference in gas concentration, and dynamic factors such as near surface wind, surface currents, sea-state and wave breaking. Air-sea fluxes are either measured in-situ by the eddy covariance method or calculated from bulk formulae. In-situ ocean flux stations are sparse and expensive. The bulk method estimates the fluxes using mean surface variables and empirical transfer coefficients. The accuracy of the estimated fluxes depend on the estimated sea surface variables and parameterization. Most bulk parameterizations rely solely on surface wind and neglect sea state and currents. Uncertainties in the surface wind and uncertainties due to neglecting other effects cause errors in the estimated fluxes and consequently in the model output (Dawe and Thompson, 2006; Wu, Zhai, and Wang, 2017).

Numerical models are unique tools used to predict the evolution of the atmosphere and the ocean. Uncertainties in operational ocean forecasts are still high (e.g. Golbeck, 2015), and part of these uncertainties are due to atmospheric forcing errors (Milliff et al., 1999). To make a prediction, a model needs to solve equations describing the physics governing the evolution of the state and to know the current state of the atmosphere and ocean (initial conditions). The main limitations of model forecasts are the approximations in the governing physics and errors in the initial conditions. The evolution of the atmosphere and the ocean is chaotic, i.e. small changes in initial conditions can have a significant impact on the subsequent evolution. This causes forecast errors that increase with time and loss of predictability (Leutbecher et al., 2017). Even if the governing equations were exact, the prediction of the atmospheric and oceanic state would be limited by the accuracy of initial conditions (Schiller and Brassington, 2011). A large part of the effort made for improving the performance of model predictions is dedicated to improving initial conditions, through making observing systems more accurate and through development of data assimilation techniques.

Data assimilation is used to estimate initial conditions for the forecast model from meteorological and oceanic observations. Modern numerical weather and ocean prediction systems make use of in-situ and satellite observations. These observations provide high resolution information of the state of the atmosphere and ocean. The impact of high-resolution satellite winds on the ocean response has been demonstrated, (e.g. Milliff et al., 1999). In particular, the high-resolution properties of satellite winds improve the representation of ocean eddies and thus contribute to more realistic ocean circulation model simulations (Kersale et al., 2010). Breivik and Sætra, 2001 showed that assimilation of high frequency coastal radar currents into a coastal ocean model yields analyses and short range forecasts that are significantly improved compared to model forecasts without assimilation.

The ocean, particularly coastal regions, is host to a variety of human activities such as fishing, ship navigation and recreation. These coastal areas are most vulnerable and exposed to man-made pollution, e.g. oil spill and plastic. Marine plastic debris floating on the ocean surface is one of the major environmental problems, but its distribution in the ocean is poorly mapped (Sebille et al., 2020). Ocean surface circulation is a key factor in the advection and dispersion of the marine pollutants (Sebille et al., 2020). Moreover, ocean currents have an effect on ship navigation. For instance, optimum routing of ships can be achieved by a numerical simulation if information about the wind, waves, and currents can be forecast in advance (Chen, Shiotani, and Sasa, 2015). The ocean is also a source of energy, e.g. tidal and wave energy. The ocean energy industry has made significant progress in recent years (Uihlein and Magagna, 2016). Currently, all ocean energy technologies except tidal can be considered at conceptual or demonstration stage. Ocean wave and tidal current energy are the two types of ocean energy which are most promising and are expected to contribute to the supply of energy in the future. Thus, observation of ocean currents, may contribute to the optimization of ocean energy exploitation, similar to offshore wind resource mapping using satellite observations of winds and prediction of the expected energy production (Hasager et al., 2015). Finally, in terms of societal impact of the ocean, with a large portion of the world's population living close to the coastline, ocean observation is essential for coastal hazards management to mitigate damage from natural hazard and extreme events, e.g. storm surges.

1.2 Ocean observation: state of the art

This thesis concerns the retrieval of surface winds and currents. Thus, only observation tools relevant for these two parameters are described.

In-situ observation

These are considered as reference data in meteorology and oceanography and often used for validation of numerical models and calibration of remote sensing data. Thus, it is important to understand the measurement principle of different in-situ sensors and their limitations. In-situ observations can be classified by sensor technology (mechanical, acoustic or optical), by the type of the sensed flow (Eulerian or Lagrangian) or by the type of the carrying platform (fixed, drifting or moving) (Joseph, 2014). Fixed sensors provide time series of the Eulerian flow. Sensors mounted on freely drifting platforms provide the Lagrangian flow. Sensors mounted on moving platforms can be considered neither true Eulerian nor Lagrangian measurements. They are sometimes called semi-Eulerian.

For ocean currents, the most common measuring sensor is the acoustic Doppler current profile (ADCP). The ADCP can be sea bottom-mounted and upward looking, vessel-mounted or moored-buoy mounted and looking upward or downward. ADCPs can also be mounted under rigs and offshore platforms at any depth. Mechanical sensors are limited by friction to slow currents, typically 1 to 3 cm/s (Joseph, 2014). Most modern installations are equipped with more sensitive and accurate acoustic or optical sensors. Drifting buoys freely follow the ocean currents and their positions are tracked using GPS. These buoys do not record measurements at a fixed location but provide Lagrangian time series of the mean motion of water particles at a given depth. The depth depends on the location of the sensor on the drogue, which is typically between 1 m and 15 m from the surface. Drifting buoys are important for studying dispersion of floating oil spills. A third category are current meters mounted on moving platforms such as ferry box systems, autonomous underwater vehicles, gliders, saildrones, marine animals.

For wind measurements near the ocean surface, the most used wind data are provided by moored buoys equipped with an anemometer (mechanical or ultrasonic). A few platforms are equipped with lidar wind profilers. Ground-based Doppler weather radars, with coverage extending to the sea, provide only the radial component of the wind at height $\sim$500 m. Thus, they are not very useful for near sea surface applications.

Remote sensing

Here, we focus only on active microwave sensors (radar). There are several radar based techniques for measuring ocean currents (Joseph, 2014; Isern-Fontanet et al., 2017; Villas Bôas et al., 2019). One of the most established techniques is using coastal high frequency (HF) radars (Barrick, 1972). The advantage of HF radars is their simplicity, but the drawback is their sparsity. The coverage is limited to some 100 km from the coastline and the spatial resolution is relatively coarse ranging from $\sim$500 m to 6 km. Another well established technique is satellite altimetry. This also has a coarse spatial resolution ($\sim$10 km) and only the geostrophic component of the ocean current can be estimated from sea surface height measurements. Marine radars (Young, Rosenthal, and Ziemer, 1985) are also used to estimate surface currents. This technique is based on deviation from the expected dispersion relationship, which is interpreted as being due to a current induced Doppler shift of the wave frequency. Synthetic aperture radar (SAR) complements these measuring techniques by offering high resolution observations of currents ($\leq$ 1 km). This is particularly important in coastal regions characterized by small scale processes. Moreover, satellite-borne SAR is not limited in spatial coverage, i.e. any region can be imaged. A single-beam SAR is limited by the fact that it provides only the radial component of the current.

Remote sensing techniques of surface currents from spaceborne SAR can be classified in two categories, feature-tracking-based or Doppler-based techniques. An ocean feature here refers to anthropogenic, e.g. oil, or biological, e.g. algae surfactants. The feature tracking technique is based on using sequential SAR images and measuring the correlation between the two images (Lyzenga and Marmorino, 1998). This measure of correlation can be related, given the time between the two acquisitions is known, to the surface motion.

The Doppler-based technique can be split in two different techniques that are quite similar in principle, but differ in design, processing and performance. A good review for sea surface currents imaging by spaceborne SAR using both techniques can be found in (Romeiser et al., 2010). The first technique is called the Doppler Centroid anomaly Analysis (DCA) and is based on the difference between the measured and the geometric Doppler centroid. The DCA was first introduced by (Chapron, Collard, and Ardhuin, 2005) and demonstrated further by (Johannessen et al., 2008; Hansen et al., 2011). The advantage of the DCA is that it requires only one SAR image. The drawback is its relatively coarse resolution ($\sim$ 1-2 km), which is still much better than the altimeter resolution and many ocean models. The second technique is based on SAR along-track interferometry which requires two SAR acquisitions with very small time difference (few miliseconds). This technique was first introduced and demonstrated by (Goldstein and Zebker, 1987; Goldstein, Zebker, and Barnett, 1989). The advantage of using ATI-SAR for sea surface current mapping is its high spatial resolution ($\sim$100 m). Such high resolution current maps would be particularly important in coastal areas, rivers, straits, etc. The drawback is the complexity of the ATI-SAR system. It requires either a single platform with two antennas or two platforms flying in tandem.

For wind measurements, the most popular remote sensing techniques are scatterometry and altimetry. Their global coverage and revisit time are suitable for synoptic and large scale studies. Note that altimeters provide only the wind speed (Witter and Chelton, 1991). Scatterometers on the other hand, carry either a rotating fan beam or multiple fixed beams. This gives them the ability to measure the wind direction in addition to wind speed (Stoffelen, 1998; Stoffelen, 2008). The wind speed is also retrieved from SAR data and in some cases the wind direction can also be extracted from SAR imagery (Horstmann and Koch, 2008).

Recently, there is an increasing number of applications requiring simultaneous data of ocean dynamics parameters. Hence an increasing need for integrated observations of surface winds, currents and waves (Villas Bôas et al., 2019). This has motivated proposals of advanced missions aiming at measuring simultaneously ocean currents, winds and/or waves, e.g. SKIM (Ardhuin et al., 2018), SEASTAR (Gommenginger et al., 2019) and WaCM (Rodríguez et al., 2019).

Why SAR for ocean remote sensing ?

SAR, like the real aperture radar (RAR), is sunlight and quasi-weather independent. The main advantage of SAR over RAR is its high spatial resolution and the fact that this resolution is independent of the distance between the sensor and the target. This allows Earth observation from space with resolutions approaching optical sensors resolutions. For a review of SAR principles and applications, see (e.g. Robinson, 2004; Moreira et al., 2013; Ulaby and Long, 2014).

Radar backscatter is sensitive to the dielectric (permittivity and conductivity) and geometric (surface roughness) properties of the illuminated surface. Over the ocean surface, the variation of the dielectric properties is relatively small. Moreover, at microwave frequencies of interest here (5-10 GHz) the radar backscatter is only weakly sensitive to temperature and salinity. Note, however, that sea surface temperature affects the backscatter indirectly by altering the surface roughness (Chelton et al., 2004). Thus, the radar is mainly used to sense the kinematic properties of the sea surface (Hasselmann et al., 1985). Finally, SAR has proven to be particularly good at imaging ocean features such as currents (Kudryavtsev et al., 2005), fronts and eddies (Johannessen et al., 1996), internal waves (Alpers, 1985), gravity waves (Alpers, Ross, and Rufenach, 1981) and shallow water bathymetry (Alpers and Hennings, 1984).

It is currently well-established that SAR can be used for sensing several ocean phenomena and for extracting several oceanic parameters. The oceanic parameters that have attracted most attention from researchers during last decades are the wave spectra (Hasselmann and Hasselmann, 1991; Engen et al., 1994) and the sea surface wind speed (Horstmann et al., 2003). From the wave spectra, several wave parameters can be extracted such as significant wave height and peak period (Schulz-Stellenfleth, König, and Lehner, 2007). The sea surface wind speed retrieval has benefited from the similarity to scatterometry, which is well established (Stoffelen and Anderson, 1993; Bentamy et al., 2017). An overview of wind retrieval from SAR can be found in (Horstmann et al., 2003; Dagestad et al., 2012). There are still a few challenges to overcome in both fields, e.g. wind and wave direction ambiguity, high wind speed and rain contamination.

Although the first demonstrations of the feasibility of sea surface current measurements using SAR have been published in the late Eighties by (Goldstein and Zebker, 1987) and (Goldstein, Zebker, and Barnett, 1989), surface currents retrievals is still an on-going and challenging research field. This is because the retrieval of surface currents, as is shown in the appended papers, is highly dependent on accurate knowledge of other meteorological and oceanic parameters, i.e. wind field and wave spectrum, in addition to platform trajectory and attitude. Note that sea surface current speed is much smaller than wind speed, which puts stringent constraints on the precision and accuracy of the measurements and retrieval algorithms. Moreover, currents are modulated by topography and interact with surface waves and this interaction is difficult to model.

1.3 Thesis objectives

The overall goals of this thesis are to improve the understanding of the relation between SAR observables and meteorological (wind) and oceanic (waves and currents) processes, in order to enhance the utilization of SAR data (backscatter and Doppler frequency shift) for optimal current and wind retrieval. The knowledge gained during this work will support the reprocessing of archived SAR data and the design of spaceborne SAR missions aiming at measuring ocean surface currents and winds. The goals of the work described in this thesis were to

- Implement a processing chain for along-track interferometric SAR data. The processor takes the pair of complex ATI-SAR images and produces calibrated backscatter and Doppler shift. This includes development and implementation of a calibration method for the Doppler shift using land as a reference.
- Analyze the variation of the processed quantities (backscatter and Doppler shift) with meteorological and oceanic parameters and understand their relationship.
- Develop and implement algorithms for the retrieval of ocean surface currents and winds from the processed SAR data using existing geophysical model functions.
- Demonstrate and assess the performance of SAR estimates of sea surface currents through case studies in the Baltic Sea region. This involves comparison of the derived currents with regional ocean circulation models and in-situ data when available.

2

Upper ocean dynamics and air-sea interaction

In this chapter a basic overview of the dynamics of the upper ocean is given. For a detailed overview of this topic, the reader may refer to the following references (Philips, 1977; Apel, 1987; Schiller and Brassington, 2011). The complexity of the ocean dynamics resides in the large range of spatial and temporal scales that can differ by orders of magnitude. The ocean dynamics is driven by processes with temporal scales ranging from a fraction of a second (e.g. ripples) to hundreds of years (e.g. climate change) and with spatial scales ranging from centimeters (e.g. turbulent eddies) to thousands of kilometers (e.g. tides). Moreover, all these oceanic processes are interacting with each other and interacting with the atmosphere.

2.1 Wind

The wind provides one of the main forces driving the upper ocean circulation. When the wind blows over water, surface friction and pressure fluctuations transfer energy from the wind to the water through wind stress (also called momentum flux). This generates surface waves and currents. Despite the rich literature on the subject, the physical mechanism for the early stage of waves generation by wind is still not fully understood. The two main explanations for wind wave generation were derived by Phillips and Miles. Phillips showed that pressure fluctuations, induced by turbulent eddies near the sea surface, cause the water surface undulations to develop and grow (Phillips, 1957). He suggested that the pressure fluctuations with size and phase velocity matching that of the free waves are amplified by a resonance mechanism. Miles suggested a mechanism based on the shear flow of the mean air velocity profile (Miles, 1957). Generally speaking, wave growth depends on wind speed, duration and fetch. The wind energy is transferred to the water until the water waves reach a maximum wave height and the growth ceases. At that stage (called fully developed sea), the wind energy input to the waves is balanced by wave-wave interaction and dissipation by wave breaking.

Ekman's theory (Ekman, 1905) is the basis of our understanding of the wind-driven upper ocean circulation. Ekman's original theory assumes uniform steady wind blowing over a homogeneous ocean having a constant eddy viscosity for a long enough time ($\geq$ 12 h depending on latitude). In this theory, the wind stress is the moving force balanced by frictional forces and the Coriolis acceleration. Moreover, the ocean surface wind plays an essential role in the exchange of heat, gases and momentum at the atmosphere-ocean interface. It is therefore crucial to accurately represent the wind forcing in numerical ocean model simulations. The air-sea fluxes are also affected by sea state (Bourassa, Vincent, and Wood, 1999) and currents (Wu, Zhai, and Wang, 2017). For instance, calculation of the air-sea CO2 fluxes depends on the wind products (Parard et al., 2017; Meyer et al., 2018).

The ocean also affects the atmospheric circulation in the marine atmospheric boundary layer (MABL) by feedback mechanisms. Several explanations are given in literature. First, the wind stress is affected by surface currents because it depends on the relative motion between the air and the sea surface and on the sea state. A second mechanism is due to horizontal sea surface temperature (SST) gradient (Chelton et al., 2004). Two main factors may explain how SST fronts induce air circulation, namely, pressure-gradient forces and horizontal variations of stability that affect mixing and thus friction at the sea surface (Bourras et al., 2004). The SST gradients induced by baroclinic currents and eddies alter the MABL stability (Bourras et al., 2004). The SST front induced pressure-gradient force generates land-sea breeze like wind circulation from cold to warm region which alters the overlying wind. The effect of SST-induced changes on wind stress depends on both the SST gradient and the wind direction relative to the gradient (Chelton et al., 2001). Finally, the near-surface air flow is also affected by the sea state. The wind blowing over waves is modulated by the underlying waves (Kudryavtsev, Mastenbroek, and Makin, 1997). The authors suggest that the variation of the wind stress along a surface long wave is due to the distortion of the flow by the long wave, and to the variation of the roughness induced by the modulated short waves. This yields a maximum of the stress located at the wave crest and minimum at the trough.

2.2 Waves

There are several types of oceanic waves, but only the ones that are relevant to radar remote sensing are discussed here, i.e. capillary waves, gravity-capillary waves, gravity waves and internal waves. Oceanic waves are usually classified by the generating force, restoring force or wavelength. The ocean waves are generally dispersive, that is waves with different wavelengths propagate with different phase speeds. The wave frequency ω (rad/s) and wavelength λ (m) are related by the dispersion relation (Kundu, Cohen and Dowling, 2016)

$$\omega = \sqrt{\left(g\,k + \frac{\sigma\,k^3}{\rho_\omega}\right)\tanh(kH)} + \mathbf{k}\cdot\mathbf{U} \tag{2.1}$$

where σ, k , g, ρ_w and H are, respectively, the water surface tension (N/m), the wavenumber $k = 2\pi/\lambda$ (m^{-1}), the acceleration due to gravity (m/s^2), the water density (kg/m^3) and the water depth (m). **k** and **U** are the wave vector and the surface velocity, respectively. The wave oscillation period is given by $T = 2\pi/\omega$.

The phase speed c_p is given by $c_p = w/k$, using equation 2.1

$$c_p = \sqrt{\left(\frac{g}{k} + \frac{\sigma k}{\rho_w}\right)\tanh(kH)} + \frac{\mathbf{k}\cdot\mathbf{U}}{k} \tag{2.2}$$

Capillary waves represent the initial stage of wave generation. They are the first waves produced by wind blowing over a flat sea, and they have a very short wavelength, $\lambda \leq 1.73$ cm, (Kundu, Cohen and Dowling, 2016). This value of λ (1.73 cm) corresponds to minimum phase velocity $c_{p_{min}}$ = 0.23 m/s. Another type of capillary waves that are relevant to radar remote sensing of the ocean surface is parasitic capillary waves (also called bound waves) (Plant, 1997; Gade et al., 1998b). These are usually trapped on the forward slope of wind-generated gravity waves. These are not generated directly by wind force.

Gravity waves are not affected by surface tension, but have gravity as the dominant restoring force. These are waves with wavelength between $\sim$7 cm and several hundred meters. In addition to their phase speed, waves induce orbital motion of the water particles. This orbital motion acts as a local current which advects the gravity-capillary and capillary waves, hence modulating their apparent frequency. The orbital velocity depends on the wave frequency ω and amplitude a (Kundu, Cohen and Dowling, 2016). For instance, a wave with an amplitude a = 1 m and ω = 0.78 rad/s, the maximum orbital velocity is u_{max} = $a \cdot \omega$ = 0.78 m/s. As mentioned before, due to dispersion, longer waves travel faster than shorter waves. As a consequence, long waves rapidly move outside the generating area and become swell. Swell has a typical wavelength that is greater than $\sim$200 m and period larger than $\sim$13 s.

Internal waves are generated in stratified water layers. The force generating these waves can be of multiple origins, but one common generation mechanism is a tidal flow over a rough topography. Internal waves are characterized by large periods $\geq$ 10 min, long wavelength (several hundred meters) and higher amplitudes than surface gravity waves. The phase speed is much smaller than surface waves ($\sim$ 30 times smaller) (Leppäranta and Myrberg, 2009). Internal waves affect the SAR backscatter signal, indirectly, by generating horizontal surface currents which modulate the surface capillary-gravity waves (Alpers, 1985). Surface currents generated by internal waves also affect the phase signal and thus the Doppler frequency shift. They generate convergence and divergence zones on the surface due to the movement of water particles. It has been shown that the resulting surface velocities can be detected by ATI-SAR (Thompson and Jensen, 1993).

An important phenomena in ocean remote sensing and air-sea interaction is wave breaking (Melville 1996). A gravity wave tends to break when it attains ka $\sim$ 0.44, i.e. a maximum amplitude $\sim 0.07\lambda$ (geometric criterion). Another criterion (kinematic criterion) is used to define wave breaking condition, which states that breaking occurs when the orbital velocity at the crest exceeds the phase speed c_p, i.e. u_{max}/c_p >0.9.

As will be explained later, radar signals interacts mainly with the so-called Bragg waves. The Bragg waves for C-band and X-band radars have wavelength λ_B equal to a few centimeters. These waves fall in the category of gravity-capillary waves, also called ripples, which are affected by both surface tension and gravity with wavelength $\lambda \leq$ 7 cm.

2.3 Currents

The velocity of sea surface currents is a combination of several components. These components can be classified by the causing force such as buoyancy (thermohaline), Moon-Sun gravity (tides), pressure-gradient (geostrophic), wind-stress (wind drift) and wave-induced (Stokes drift). Note that the pressure gradient can also be a result of wind blowing in the same direction during a long enough time and piling up water mass. Similarly, the wave-induced current is initially generated by the wind.

Thermohaline circulation is formed in the presence of density gradients in the ocean, i.e. differences in temperature and salinity. The driving force is the generation of potential energy by the sea surface heating in combination with mixing. This circulation is usually much slower compared to wind-driven currents.

The wind-driven currents can be classified into geostrophic and ageostrophic currents which include Ekman current (Ekman, 1905) and non-Ekman components, e.g. inertial current. The Ekman current is the direct response of the upper water layer to the local wind stress balanced by the Coriolis "force". It is a short term phenomenon (few hours to $\sim$day). The geostrophic current is a relatively long-term phenomenon characterized by a slow response to wind variation. In this case the motion is governed by a balance between the pressure gradient force and the Coriolis force. An Ekman current can develop into, if conditions in terms of basin size and wind duration are met, a geostrophic current.

In linear wave theory, by definition, waves transport energy but not water mass. By this definition, the average, over the wave period, of the velocity of a water particle riding the free surface of the wave is zero. This is, however, not true in finite amplitude wave theory or Stokes' theory. Stokes drift (Stokes, 1847) is defined as the net velocity experienced by a water particle in the direction of wave propagation (in the absence of any other current). The formal definition is the difference between the average Lagrangian flow velocity of a fluid particle and the average Eulerian flow velocity of the fluid.

Sometimes in the literature, the sum of wind- and wave-induced components is referred to as the total surface drift current. Estimation of the surface drift current, its relation to the wind and the contribution ratio of waves has been, and still is, a topic of research. Many authors, (e.g. Wu, 1983; Jenkins, 1987; Rascle et al., 2008; Ardhuin et al., 2009) have investigated this topic theoretically and experimentally, and different results have been reported with clear regional dependencies. However, a rule of thumb often used in the literature is that the surface drift is $\sim 2-3\%$ of the wind speed and the direction is $10-45^o$ to the right of the wind in the Northern hemisphere (Wu, 1983; Jenkins, 1987; Ardhuin et al., 2009). There is a debate about how the Stokes drift affects radar measurements. Some authors, (e.g. Röhrs et al., 2015), concluded from their experiment that Stokes drift does not contribute to the radar measurements.

Tides are global scale oceanic phenomena generated by the gravity of the moon and the sun, combined with a rotating Earth. They can be classified as global scale waves, but on the local scale, tides are seen as vertical motion of the sea level (tide range) and horizontal motion of water. Tidal currents, also called tidal flow or stream, refer to the periodic horizontal movement of water driven by the sea level rise induced by the tides. Thus, the velocity of the tidal current is directly related to the tide range. These currents are affected by the topography and the size of the water body. That is, they are stronger in some geographic areas than others. In open ocean, such as the Atlantic and Pacific, the tides are stronger than in smaller basins such as the Mediterranean and Baltic sea. These small basins do, generally, not generate their own tides, but the Atlantic ocean tide can penetrate into them through straits.

2.4 Eddies and fronts

Oceanic eddies and fronts are ubiquitous features of ocean circulation, and play an important role in the air-sea interaction. Oceanic fronts occur at the boundaries between two distinct water masses with one or more different properties, e.g. velocity, temperature, salinity, etc. Depending on the motion direction of the two water masses, a front may be convergent or divergent.

Eddies denote circular motion of the water (swirling). Instabilities in the oceanic fronts generate meanders. These meanders usually grow and detach from the current to form eddies.

Eddies are usually classified into mesoscale with a radius about 40-100 km (depending on latitude) and submesoscale eddies with a diameter of up to 10 km. These submesoscale ocean eddies only exist for a few hours or days (Schiller and Brassington, 2011).

Oceanic fronts and eddies are often associated with changes in sea surface roughness. This allows imaging sensors such as SAR to detect these features, (e.g. Vesecky and Stewart, 1982; Johannessen et al., 1996; Johannessen et al., 2005). The detection of the surface roughness changes are due to three main mechanisms: accumulation of surfactants in regions of converging surface currents, the interaction of surface waves directly with surface current gradients and atmospheric stability effects associated with the surface temperature gradients discussed earlier.

2.5 Baltic Sea circulation

Since most of the case studies investigated in this work are based on satellite data acquired over the Baltic Sea region, a brief description of its circulation is given in this section. For a thorough description, the reader is referred to (Leppäranta and Myrberg, 2009; Omstedt et al., 2014).

The Baltic Sea is an intra-continental brackish sea with an average residence time $\sim$30 years (Omstedt et al., 2014; BACCII author team, 2015). It is a relatively shallow sea with an average depth of $\sim$50 m. The only exchange between the Baltic proper and the North sea, through the Kattegat and Skagerrak Seas, is via the Danish straits and Öresund. The fresh water flows out as a thin layer above the dense salty water through the Öresund and the Danish belts. Salty water flows in from the Atlantic ocean into the Baltic Sea where the fresh water mixes with the sea water. This forms the so-called *Baltic haline conveyor belt* (Döös, Meier, and Döscher, 2004).

The Baltic Sea does not generate its own tide due to its limited size. Moreover, the Kattegat and the Danish straits are relatively narrow and shallow which limits the penetration of the oceanic tides. Since the tide velocity is related to water level changes, with amplitudes around 10 cm, very weak tidal currents are observed in the Baltic Sea (Leppäranta and Myrberg, 2009). However, seiches are common and can reach higher amplitudes.

The size of the Baltic Sea basins are relatively small and strong wind duration is short, hence the growth of waves is limited. Wave statistics show that the significant wave height is less than 2 m and with periods less than 7 s in 90% of the cases (Leppäranta and Myrberg, 2009). Thus, high amplitude waves and long-period swell are rare in the Baltic Sea. The Baltic Sea with a stable stratification, provides a background for internal waves development. Thus, these are commonly observed.

Finally, the Baltic Sea has no noticeable permanent and stable current structures such as the Gulf stream in the Atlantic ocean. There is, however, a net (long term mean) flow generating a large and slow southerly coastal current along the Swedish coast (Leppäranta and Myrberg, 2009). These currents are very weak with a mean average speeds of $\sim$ 5 cm s^{-1}. Wind driven currents are usually stronger and reach $\sim$ 50 cm s^{-1} (Leppäranta and Myrberg, 2009).

Synthetic aperture radar (SAR)

3

3.1 SAR principles

SAR is an imaging radar on board a moving platform (typically an aircraft or a satellite). It can be deployed in several imaging modes depending on possibilities to steer the antenna beam. The geometry depicted in Figure 3.1 illustrates the side-looking stripmap mode with a linear platform track. In this mode the look angle is fixed while the antenna footprint is sweeping the illuminated area. For simplicity, only this imaging mode is considered in this chapter.

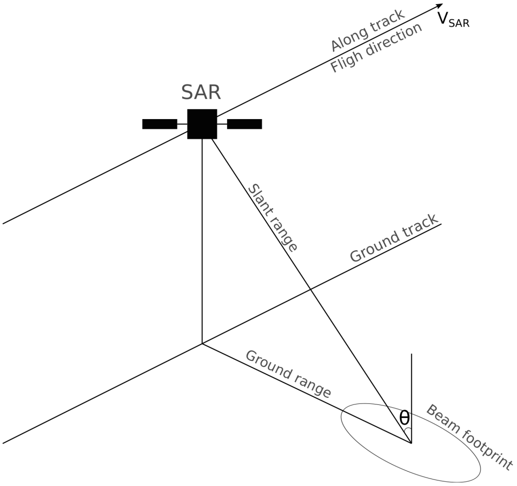

Figure 3.1. *Stripmap side-looking SAR.* V_{SAR} *is the speed of the SAR platform and* θ *is the incidence angle.*

There is abundant literature about SAR, its processing algorithms and applications, see for example (Cumming and Wong, 2005; Richards, 2005; Moreira et al., 2013; Ulaby and Long, 2014). The flight direction is denoted as azimuth or along-track and the look direction is denoted as line-of-sight (LOS), slant range or radial direction. The main difference between SAR and RAR is the spatial resolution in the along-track direction, hence only this aspect is discussed here. In short, SAR is a technique (system + processing) to overcome the beam-limited resolution in the along-track direction. The angular beam-limited resolution ($\theta_a = \lambda/D$) is determined by the wavelength λ and the antenna length in the along-track direction D. From this point of view, SAR is very similar in concept to aperture synthesis using an array of antennas.

According to the diffraction limit, the resolution can only be improved by increasing the frequency or the antenna size. SAR works around this, by transmitting and recording coherently the scattered signal (amplitude and phase) from the targets illuminated by the antenna beam at each position on its track separated by a distance V_{SAR}/PRF, where V_{SAR} is the speed of the platform and PRF is the pulse repetition frequency. The recorded signals are coherently integrated after compensation for the phase due to the varying distance to the target, which is due to the motion of the platform (assuming static ground). This is equivalent to a long linear antenna array (synthetic aperture) of length D_{SAR}, with the main beam of the array pointing in the broadside direction toward the target location.

The achieved spatial resolution in the along-track direction is given, for both SAR and RAR, by (Richards, 2005)

$$\delta_{SAR} = \frac{R\,\lambda}{2\,D_{SAR}} \tag{3.1}$$

$$\delta_{RAR} = \frac{R\,\lambda}{D_{RAR}} \tag{3.2}$$

Note that the resolution of SAR relative to a real antenna array of the same size is improved by a factor 2. Note also that the synthetic aperture length increases with range, which yields δ_{SAR} independent of R. SAR has also some constraints. The PRF needs to be high enough, usually much higher than that of the RAR, to avoid azimuth ambiguities. On the other hand, this constraint limits the ground coverage in the range direction to avoid range ambiguity. Other advanced imaging modes, e.g. ScanSAR or TOPS, are used to overcome this constraint, but at the expense of along-track resolution.

3.2 Doppler centroid

Estimation of the focusing parameters is essential in SAR processing (Cumming and Wong, 2005). The accuracy of these parameters affects the SAR image quality and the Doppler analysis for geophysical applications. The Doppler frequency shift is the difference between the frequency of the received signal compared to the frequency of the transmitted signal, due to the relative motion between the antenna and the target. SAR imaging in the azimuth direction requires a relative motion between the platform and the target. The Doppler frequency at the centre of the antenna beam is called the Doppler centroid (DC). The difference between the maximum and minimum Doppler frequencies is called the Doppler bandwidth (B_D).

For an airborne SAR moving in a linear track at constant altitude, the Doppler frequency of a given static target varies with azimuth time (called slow time). For a side looking SAR, i.e. antenna look direction perpendicular to the flight direction, the DC is (ideally) zero if the illuminated target is static, but a non-zero DC occurs either by a moving target or due to antenna rotation (squint). Figure 3.2 depicts schematically the variation of the signal amplitude, Doppler frequency and the total Doppler spectrum for a side-looking SAR illuminating a static or moving target. It can be noticed that a squinted antenna beam illuminating a static surface would yield similar effect as non-squinted beam illuminating a moving surface. If the amount of the squint is unknown or not taken into account, the derived Doppler centroid will be biased.

For spaceborne SAR, the Earth rotation must be taken into account. In order to obtain a zero DC, the antenna look direction needs to be perpendicular to the relative velocity of the SAR and rotating Earth. Most modern SAR platforms employ yaw steering technique (Raney, 1986; Fiedler

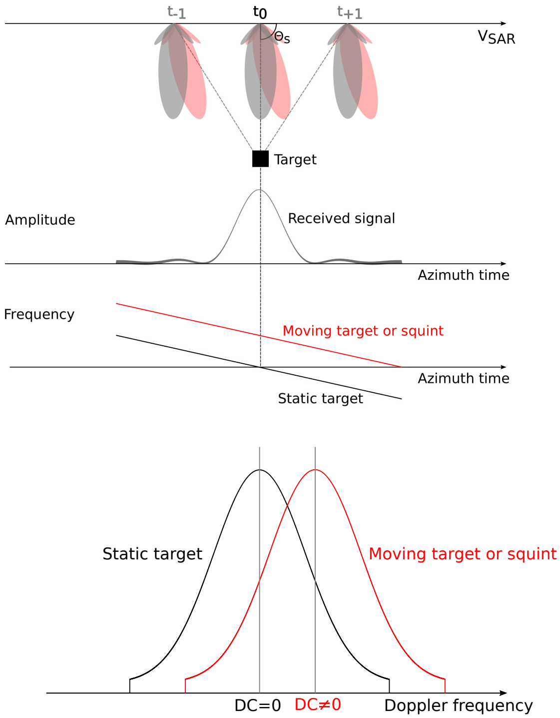

Figure 3.2. *SAR Doppler centroid shift due to a moving target or squinted antenna beam ($\theta_s \neq 0$).*

et al., 2005) in order to minimize and maintain the Doppler centroid within the unambiguous Doppler bandwidth ± PRF/2. In geophysical applications, the DC estimated for a static surface is sometimes called the geometric DC since it is due to the geometry of the acquisition and independent of the scatterer motion (in Earth-fixed coordinate system).

Assuming a circular orbit, the Doppler centroid is given by (Raney, 1986)

$$DC = \frac{2V}{\lambda} \sin\gamma \cos a \left[1 - \frac{\omega_E}{\omega}(\cos\beta \sin i \tan a + \cos i)\right] \tag{3.3}$$

where V is the satellite speed, β and i are the argument of latitude and inclination of the satellite orbit. ω_E and ω are the Earth and satellite angular velocities. γ is the elevation angle and a is the azimuth angle (measured in the horizontal plane) from flight direction, also called yaw angle. See the geometry in Raney, 1986.

The Doppler bandwidth is given by

$$B_D = \frac{2V}{\lambda} \Delta\theta_a \sin a \left[1 + \frac{\omega_E}{\omega}(\cos\beta \sin i \cot a - \cos i)\right] \tag{3.4}$$

where $\Delta\theta_a$ is the antenna azimuth beamwidth (assumed small).

Since, according to equation 3.3, the geometric DC varies with latitude and varies with elevation angle, it is difficult to achieve and maintain zero DC along the satellite orbit over the whole swath. Thus, a residual geometric DC is usually present and needs to be estimated for both processing and geophysical analysis. It can be estimated using the platform orbit and attitude data or from the signal itself (Madsen, 1989; Wong and Cumming, 1996). Experiments show that for geophysical applications, even with the use of yaw-steering, the accuracy of the satellite position, velocity and attitude, is usually not good enough to predict accurately the geometric DC, (e.g. Hansen et al., 2011).

3.3 SAR interferometry

RAR locates the origin of the signal (target) in an iso-range-sphere using the time delay, SAR adds a second dimension by locating the target in the azimuth direction using the Doppler shift. The intersection of the iso-range sphere and the Doppler cone is a circle. The iso-range sphere is centered at the antenna and the Doppler cone has its axis in flight direction. A single SAR antenna is not able to locate the target in that iso-range-Doppler circle, i.e. the angle in the plane perpendicular to the flight direction is undefined. Because all the targets in that circle have the same Doppler shift. Interferometric SAR (InSAR) adds a third dimension by locating the target in elevation and determines this angle. This requires at least two SAR acquisitions, of a common observed area, separated in space or time.

In SAR, the phase of the signal is directly measurable from the complex image. The phase ϕ of a single SAR measurement is related to the path length R as $\phi = -2k_e R + \phi_0$ (Hanssen, 2001), where $k_e (= 2\pi/\lambda_e)$ is the radar wavenumber and ϕ_0 is the scattering phase. The main assumption in InSAR is that the scatterer distribution within the pixel do not change, i.e. ϕ_0 is constant between acquisitions. Actually, InSAR still works if ϕ_0 changes slightly, the degree of random change of ϕ_0 is measured by the *coherence*.

InSAR can be classified into across-track interferometry where the two acquisitions differ in elevation angle and along-track interferometry where the two acquisitions differ in time. InSAR can also be classified, depending on time separation between acquisitions, into single-pass interferometry and repeat-pass interferometry. In the following, only the single-pass configuration is considered. In this configuration, the two antennas can be mounted on the same platform or on separate platforms. The separation between the antennas is called the baseline, where the choice of the baseline is application dependent. When the two platforms are close enough, bistatic imaging can be used, i.e. one transmitter and two receivers. Otherwise, monostatic imaging is used, i.e. each platform has its own transmitter and receiver. Overviews of SAR interferometry can be found in Bamler and Hartl, 1998; Rosen et al., 2000; Hanssen, 2001.

3.3.1 Across-track interferometry

The main application of across-track interferometry is the estimation of surface elevation to construct a digital elevation model (DEM). To achieve this, two antennas must be separated in the across-track direction, illuminating the same area on the ground with slightly different viewing angles, as illustrated in Figure 3.3. The interferometric phase ϕ_{int}, i.e. the phase difference between the two acquisitions, at each pixel is related to the difference in range ΔR (Bamler and Hartl, 1998; Rosen et al., 2000)

$$\phi_{int} = \phi_1 - \phi_2 = n\, k_e\, \Delta R + m\, 2\pi \tag{3.5}$$

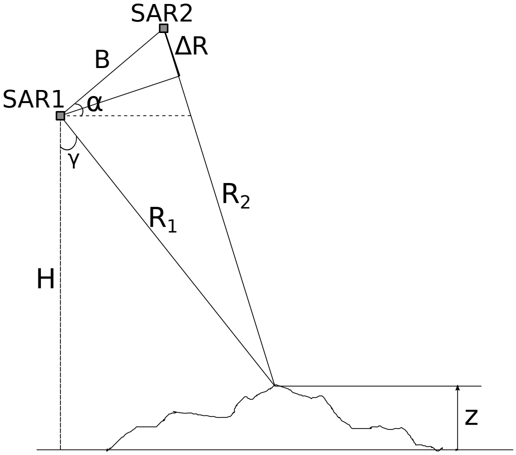

Figure 3.3. *The geometry of across-track interferometry. The flight direction is into the page. The antenna beam is looking to the right of the flight direction. Flat Earth is assumed.*

where $n = 1$ for bistatic and $n = 2$ for monostatic mode and m is an integer. Given that the positions of the platforms are known and the range to the target is measured from each platform, the target height can be estimated from the measured phase. Assuming $B << R$, ΔR is related to the elevation angle γ by (Rosen et al., 2000)

$$\Delta R = B\ sin(\alpha - \gamma) \tag{3.6}$$

Then solving for the height z becomes a geometric problem

$$z = H - R\ cos\gamma \tag{3.7}$$

To summarize, ΔR is determined from the phase using equation 3.5, and given B and α calculated from the positions of the platforms, γ and hence z can be determined from equations 3.6 and 3.7, respectively. Note that the sensitivity of ΔR, hence the phase, to height is determined by the baseline B. Thus a larger baseline provides a better sensitivity to elevation. A larger baseline, however, reduces the coherence which becomes zero at the critical baseline (Hanssen, 2001).

3.3.2 Along-track interferometry

The objective of along-track interferometry (ATI) is to measure the motion of the surface or an object. The concept consists of acquiring two images of the same patch of ground at two different times as illustrated in Figure 3.4. The optimal time delay between the two acquisitions is based on the velocity of the target we want to measure and the correlation time of the imaged surface. Recall that InSAR is based on the assumption of constant scattering phase. This assumption is not valid when imaging non-rigid surfaces such as natural scenes. In oceanographic applications, the decorrelation time of the ocean is short, thus the interferometric time delay should be of the order

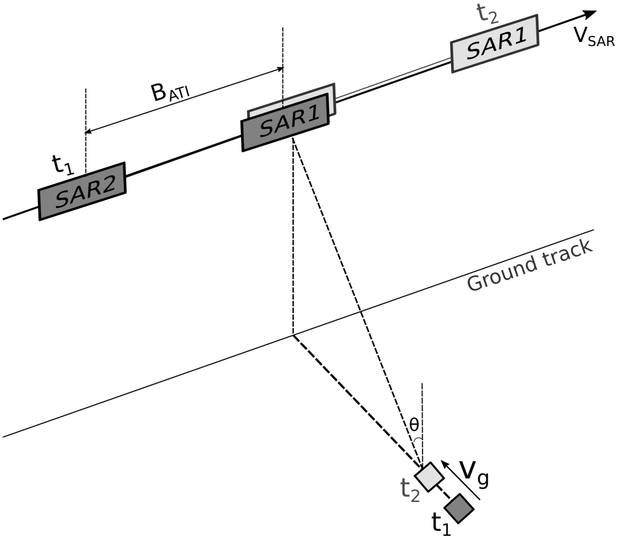

Figure 3.4. *The geometry of along-track interferometry. V_g is the ground range velocity of the target, e.g. an ocean surface patch, and θ is the incidence angle.*

of 10 milliseconds for microwaves depending on the sea state (Tucker, 1985). The ATI phase is directly related to the radial velocity V_r of the ocean patch (Ulaby and Long, 2014)

$$\phi_{int} = n\, k_e\, \frac{B_{ATI}}{V_{SAR}} V_r \tag{3.8}$$

where B_{ATI} and V_{SAR} are the ATI baseline and the SAR velocity, respectively. Similarly to across-track InSAR, the sensitivity of the phase to velocity depends on the baseline. Thus, longer baselines provide higher sensitivity to motion. On the other hand, a too long baseline increases the time delay and consequently decreases the *coherence*, i.e. increases phase noise. Therefore, a compromise between coherence and sensitivity must be found. Note finally, that ATI only allows measurement of the target velocity in the line-of-sight or radial direction.

3.4 Data processing - briefly

SAR data are commonly provided in the Single Look Complex (SLC) format. The backscatter σ^0 is calculated and corrected for the noise as follows (Eineder, Fritz, and Mittermayer, 2008)

$$\sigma^0(\theta) = K|DN|^2 \sin(\theta) - NESZ(\theta) \tag{3.9}$$

where K is the calibration factor, which groups all the radar equation parameters and is usually provided in the SAR auxiliary data. DN is the image pixel digital complex number measured in amplitude. θ is the incidence angle. $NESZ$ is the noise equivalent sigma zero. Equation 3.9 assumes that azimuth slope is negligible. Multi-looking is applied to the intensity image $|DN|^2$

to reduce the speckle noise. This improves the radiometric resolution but degrades the spatial resolution. The number of necessary looks is application dependent.

Interferogram processing consists of the following steps. 1) the two complex focused SAR images are co-registered in space. 2) the non-overlapping parts (between the two acquisitions) in the azimuth and range spectra are filtered out. This is called common band filtering. In case of TanDEM-X Coregistered Single look Slant range Complex data, these first two steps (co-registration and common band filtering) have already been done. 3) formation of the interferogram by multiplying one image by the complex conjugate of the other ($I = S_1 S_2^*$). 4) Estimation of the phase and the coherence. 5) removal of the flat Earth phase (interferogram flattening). This step requires accurate knowledge of the positions of the two platforms. 6) phase unwrapping is performed. 7) the image is mapped from SAR coordinates to Earth geographic coordinates (geocoding). The interferogram is defined as the complex correlation of the two images as

$$\gamma = \frac{E\{S_1 S_2^*\}}{\sqrt{E\{|S_1|^2\}E\{|S_2|^2\}}} \tag{3.10}$$

where E denotes ensemble averaging. It is replaced by spatial averaging assuming that the phase is homogeneous in a small area around the pixel of interest. The interferometric phase ϕ_{int} is defined as the argument of γ and the coherence as its magnitude. In ocean applications, an additional filtering stage, e.g. median filter, is needed to filter out targets such as ships and wind turbines in the sea. For velocity retrieval, the phase is calibrated if land is present in the image. Finally, the phase is converted to Doppler frequency shift as

$$f_D = \frac{1}{2\pi}\frac{\phi_{int}}{\tau} \tag{3.11}$$

where τ is the temporal baseline (τ=B_{ATI}/V_{SAR}), and the Doppler shift is converted to radial velocity by

$$V_r = \frac{\pi}{k_e} f_D \tag{3.12}$$

The ground range velocity V_g is related to the radial velocity by the incidence angle

$$V_r = V_g \cdot \sin\theta \tag{3.13}$$

3.5 TanDEM-X mission

TerraSAR-X/TanDEM-X is a high-resolution interferometric SAR mission of the German Aerospace Center (DLR) (Krieger et al., 2007). The mission concept is based on an extension of the existing TerraSAR-X mission by a second satellite. Both instruments are almost identical in design and operate at X-band ($\sim$ 10 GHz). TerraSAR-X was launched on 15 June 2007 and TanDEM-X was launched on 21 June 2010. The main application of the TanDEM-X mission is building a global DEM. The main orbital and system parameters are given in Table 3.1.

Flying these two satellites in a close formation provides a flexible single-pass SAR interferometer configuration with configurable baseline according to the specific needs of the application. The two satellites orbit in a helix formation, which enables a safe operation of close formation with minimum collision risk (Krieger et al., 2007). The TerraSAR-X/TanDEM-X interferometer

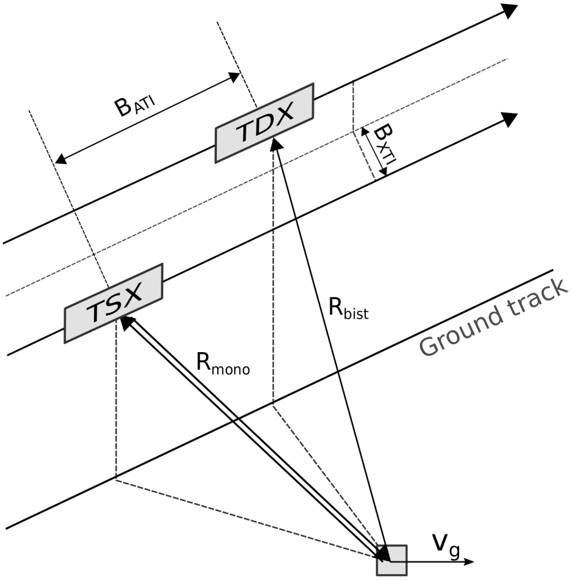

Figure 3.5. *TanDEM-X: a hybrid, single-pass and bistatic interferometric SAR.*

is, by construction, a hybrid system, i.e. a system that combines across-track and along-track InSAR as illustrated in Figure 3.5. The two satellites can operate in three different modes: bistatic mode, pursuit monostatic mode and alternating bistatic mode. The data used in this thesis are from the bistatic mode.

Orbital parameters		**System parameters**	
Orbit height	514 km at equator	Frequency	9.65 GHz
Orbit period	94.79 min	Range bandwidth	150 MHz
Repeat cycle	11 days	Azimuth bandwidth	2765 Hz
Inclination	97.44°	Range resolution	1.17 m (slant)
Asc. node / equ. crossing time	18:00 (local time)	Azimuth resolution	3.29 m

Table 3.1. *TanDEM-X orbital and system parameters for the stripmap mode (https://directory.eoportal.org/web/eoportal/satellite-missions/t/tandem-x).*

3.6 Sentinel-1 mission

Sentinel-1 is a European Space Agency (ESA) mission, which consists of a series of satellites. So far, two of these satellites have been launched. Sentinel-1A and 1B were launched on 03 April 2014 and 22 April 2016, respectively. Sentinel-1 carries a single C-band SAR instrument operating at a centre frequency of 5.405 GHz. It includes a right-looking antenna providing fast scanning in elevation and azimuth. Sentinel-1 operates in four acquisition modes: Stripmap (SM), Interferometric Wide swath (IW), Extra-Wide swath (EW) and Wave mode (WV). The data used in this thesis are from the IW mode, thus only this mode is described here. The IW mode provides a large swath width (250 km) with a moderate spatial resolution (5 m by 20 m). The IW mode images three sub-swaths using Terrain Observation with Progressive Scans SAR (TOPSAR). With the TOPSAR technique, in addition to steering the beam in range as in ScanSAR, the beam is also electronically steered from backward to forward in the azimuth direction for each burst. The main orbital and system parameters are given in Table 3.2.

Orbital parameters		**System parameters**	
Orbit height	693 km at equator	Frequency	5.405 GHz
Orbit period	98.6 min	Range bandwidth	0-100 MHz
Repeat cycle	12 days	Azimuth bandwidth	313-327 Hz
Inclination	98.18°	Range resolution	5 m (slant)
Asc. node / equ. crossing time	18:00 (local time)	Azimuth resolution	20 m

Table 3.2. *Sentinel-1 orbital and system parameters for the IW mode (https://directory.eoportal.org/web/eoportal/satellite-missions/c-missions/copernicus-sentinel-1).*

Microwave backscattering from the ocean surface

4

We limit this text to aspects related to the monostatic SAR ocean-imaging problems that are discussed or mentioned in the appended papers. A thorough description can be found in (e.g. Plant, 1990; Robinson, 2004; Ulaby and Long, 2014).

A given random surface above a homogeneous dielectric volume is basically defined by three parameters: 1) the complex dielectric constant (permittivity and conductivity); 2) roughness (height standard deviation and correlation length); and 3) slope (local incidence angle). A surface is classified as conductor or dielectric depending on the first parameter; and classified as smooth, slightly rough or rough depending on the second and third parameters compared to the radar wavelength. The scattering mechanism can be classified into three categories: specular, diffuse and resonant. For a given dielectric constant, if the roughness is small relative to the wavelength (smooth surface), the dominant scattering mechanism is specular. If the roughness is large relative to the wavelength (rough surface), the dominant scattering mechanism is diffuse. If the surface contains periodic gratings, it gives a resonant scattering, i.e. the scattering is enhanced in given directions due to constructive interference. In a real ocean surface, the scattering is a combination of all these mechanisms. However, one mechanism may dominate the others depending on the surface type, frequency, polarization and incidence angle.

4.1 Normalized radar cross section

The concept of the radar cross section (RCS, σ) and the normalized radar cross section (NRCS, σ^0), also called backscattering coefficient or backscatter, is described in detail in many text books, (e.g. Skolnik, 1970; Richards, Scheer, and Holm, 2010; Ulaby and Long, 2014). The RCS is used to characterize the properties of the target illuminated by the radar. It is a measure of the reflective strength of a target. The formal definition of the radar cross section for a point target, valid in the far field, is (Richards, Scheer, and Holm, 2010)

$$\sigma = \lim_{R \to +\infty} 4\pi R^2 \frac{|E_s|^2}{|E_i|^2} \tag{4.1}$$

where E_s and E_i are the scattered and the incident electric fields, respectively. The unit of σ is m^2. It depends on the radar frequency, electromagnetic and geometric properties of the target and the range to the target.

For distributed targets such as the ocean surface, it is convenient to use the normalized radar cross section (NRCS or RCS per unit area) $\sigma^0 = \langle\sigma\rangle/A$, σ^0 is thus dimensionless. For an imaging radar such as SAR, A is the ground resolution cell defined as $A = \delta_r \delta_{az}$, where δ_r and δ_{az} are the ground range and azimuth resolution, respectively.

4.2 Backscattering models

Calculation of the σ^0 for a given surface requires a scattering model. A number of models have been developed in the last decades for the backscattering of electromagnetic waves from the ocean surface, see (e.g. Elachi and Brown, 1977; Valenzuela, 1978; Plant, 1986a; Voronovich, 1994; Romeiser, Alpers, and Wismann, 1997; Plant, 2002; Kudryavtsev et al., 2003). The most popular models are: the specular point model valid at low incidence angles $0-20^o$ or very large slopes (Barrick, 1968), the Bragg model valid in intermediate incidence angle $20-60^o$ (Wright, 1966) and the two-scale model (Valenzuela, 1978) that combines the scattering from small scale (Bragg waves) and large scale ocean waves. A brief discussion of scattering models is given in the following sections, the reader may refer to (e.g. Valenzuela, 1968; Valenzuela, 1978; Ulaby, Moore, and Fung, 1986; Ulaby and Long, 2014) for more details.

Specular scattering model - Geometrical optics

At low incidence angles (θ <20°) specular scattering is dominant, thus specular point model can be used to simulate σ^0 (Barrick, 1968). This model is applicable to a gently undulating rough surface where the local radius of curvature ρ is much larger than the radar wavelength ($\rho k_e \cos(\theta)^3 >> 1$). According to this model, the surface is composed of plane facets and only facets tilted to be normal to the incident wave contribute. The backscatter may be calculated using geometrical optics approximation (GO), also called tangent plane approximation. The GO model is the high-frequency limit of the physical optics (also called Kirchhoff approximation) model and reads (Valenzuela, 1978)

$$\sigma^0(\theta, \varphi) = \pi \sec^4 \theta \, |R(0, \epsilon_r)|^2 \, p(\zeta_x, \zeta_y) \tag{4.2}$$

where $R(0, \epsilon_r)$ is the Fresnel reflection coefficient for normal incidence, ϵ_r is the dielectric constant, θ is the incidence angle and $p(\zeta_x, \zeta_y)$ is the joint probability density of the sea surface slopes. The dependence on wind seed and direction is implicitly included in $p(\zeta_x, \zeta_y)$. The Fresnel reflection coefficient is sometimes replaced by an effective reflection coefficient to take into account the roughness of the facets (Valenzuela, 1978). Finally, note that this model is essentially independent of frequency and polarization.

Bragg scattering model

It is well known that the main contribution to the backscattered radar signal, at moderate incidence angles (20-60^o), is due to the Bragg scattering mechanism (Crombie, 1955; Wright, 1966; Plant, 1990). That is, if the ocean surface roughness is decomposed into its Fourier components, the backscattering is dominated by the surface Fourier component satisfying the Bragg condition (Robinson, 2004)

$$k_B = 2k_e \sin \theta \tag{4.3}$$

where k_B and k_e are the ocean waves and the electromagnetic wavenumbers, respectively. For microwaves, Bragg scattering originates from the gravity-capillary waves. For TanDEM-X and Sentinel-1, the Bragg wave, at $\theta = 35^o$, will have a wavelength λ_B of 2.71 cm and 4.83 cm, respectively.

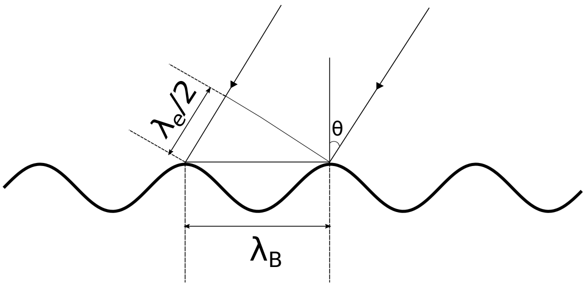

Figure 4.1. *Bragg scattering mechanism.*

This model, also called small perturbation model (SPM), assumes that surface slopes are small and surface heights are small compared to the electromagnetic wavelength; and multiple scattering and shadowing are negligible. The first and second conditions are generally satisfied in absence of long waves. The third and fourth conditions limit the applicability to moderate incidence angles. According to this model, the backscatter is proportional to the spectral density of the Bragg resonant waves and is given by (Wright, 1966; Valenzuela, 1978; Plant, 1990)

$$\sigma_B^0(\theta,\varphi) = 16\pi k_e^4 \cos^4\theta |g_{pp}(\theta,\epsilon_r)|^2 \Psi(k_B,\varphi) \tag{4.4}$$

where g_{pp} is the scattering coefficient, the subscript pp refers to polarization (VV or HH), Ψ is the 2D wavenumber spectrum of the ocean surface evaluated at k_B and φ is the antenna azimuth angle. The dependence on wind speed and direction is implicitly included in Ψ.

Since SAR measures mainly the backscatter of the Bragg waves (Plant, 1990), in absence of this component, the scattering is quasi-specular. Note that the slopes of the longer waves are usually too small, rarely exceeding 20^o (Cox and Munk, 1954), to induce specular scattering at moderate incidence angles. This is, for instance, confirmed by observation of images of the sea surface covered by oil films that dampens the ripples and dramatically reduce the backscattered power (Gade et al., 1998a). Note, however, that these Bragg waves are advected, modulated, strained, stretched, etc. by longer waves and currents. This is how these large features are detectable by SAR (Alpers, Ross, and Rufenach, 1981).

Composite surface model

This is probably the most frequently used model in remote sensing of the ocean surface. It is also called two-scale model (Wright, 1968; Bass et al., 1968; Valenzuela, 1978). As mentioned earlier, the pure Bragg scattering theory is not applicable in the presence of long waves (few times longer than Bragg waves) with heights larger than the electromagnetic wavelength. The composite surface model takes into account the effect of the long waves which consists of tilting the small scale Bragg waves.

According to this model, the surface roughness may be divided into a large scale part that has large radius of curvature and a small scale part that satisfies the Bragg condition. The large scale surface is divided into patches (facets) approximated by slightly rough planes. The pure Bragg theory is applied to each patch. Assuming the patches are uncorrelated, the resultant cross section of the two-scale surface is calculated by integrating the cross sections of single facets over the probability distribution of the long waves slopes $p(\zeta_x, \zeta_y)$ as (Valenzuela, 1978)

$$\sigma^0(\theta, \varphi) = \iint \sigma_B^0(\theta_l, \varphi)\, p(\zeta_x, \zeta_y)\, d\zeta_x d\zeta_y \tag{4.5}$$

where $\sigma_B^0(\theta_i)$ is the Bragg backscatter, θ_l is the local incidence angle, i.e. including the tilting due to the long waves and $p(\zeta_x, \zeta_y)$ is the joint probability density of slopes for the large scale part of the surface roughness.

Another approach for deriving the two scale model is based on Taylor expansion of the backscatter, to the second order, in tilting waves slopes. Such approach, sometimes called advanced two-scale model, was adopted in (Plant, 1986b; Romeiser, Alpers, and Wismann, 1997; Kudryavtsev et al., 2003). The advantage of these models is that, in addition to the tilting effect, they introduce a term representing the hydrodynamic effect (discussed later).

It has been proven that the vertical polarization backscatter (σ_{VV}^0) is relatively well explained by the composite surface model, over the range of incidence angles from approximately 20° to 60°, (e.g. Donelan and Pierson, 1987). The horizontal polarization σ_{HH}^0, on the other hand, has been underestimated by the composite-surface model, particularly at incidence angles larger than ∼45° (Plant, 2003). Thus, the composite surface model overestimates the polarization ratio ($\sigma_{VV}^0/\sigma_{HH}^0$). This has been shown in many experiments, (e.g. Mouche, Hauser, and Kudryavtsev, 2006, paper B). This discrepancy between the model and data has motivated researchers to find explanations in non-Bragg scattering mechanisms, (e.g. Mouche, Hauser, and Kudryavtsev, 2006). Plant proposed that bound tilted short waves produced by longer waves exist on the sea surface and that scattering from these bound waves can account for part of the under-prediction of σ_{HH}^0 (Plant, 1997). Other authors proposed a model, based on the composite surface model, that takes into account scattering from breaking waves (Kudryavtsev et al., 2003). This latter model also takes into account the effect of parasitic capillary waves.

Another issue with the composite surface model is the behavior of the backscatter versus azimuth with respect to the wind direction. A common used measure of model performance in this context is upwind/downwind (UD) and upwind/crosswind (UC) asymmetry. The standard (without hydrodynamic modulation) composite surface model does not reproduce the UD asymmetry observed in the data, but it reproduces the UC asymmetry. The advanced composite surface models (Plant, 1986b; Romeiser, Alpers, and Wismann, 1997; Kudryavtsev et al., 2003) on the other hand reproduce both asymmetries.

Unified scattering models

The weakness of the composite surface model is that the results can depend on the way the wave spectrum is divided into the large and small scale components, i.e. the dividing wavenumber needs to be specified. The so-called unified models, combine the Bragg scattering theory with the GO approximation to describe the scattering both at small and large scales using a single theoretical expression. One of the most known among these models is the small slope approximation (SSA) model (Voronovich, 1994). This model assumes that surface roughness has small slopes. There are other well known models of this type, e.g. the integral equation model (IEM) (Fung, 1994) and weighted curvature approximation (WCA) (Elfouhaily and Guérin, 2004). The description of these models is beyond the scope of this text. The reader may refer to the references above for more details.

Empirical models

Empirical models also called geophysical model functions (GMF), are built using a large number of collocated observations (airborne or spaceborne) of radar backscatter and in situ buoy data and/or numerical weather prediction (NWP) model data. Thus they are instrument-dependent, i.e. frequency and polarization dependent. We limit this discussion to C- and X-band GMFs that are relevant to this work.

Most of these GMFs describe σ^0 for a given polarization by a nonlinear mapping function of the incidence angle, wind speed, and wind direction, which is given as

$$\sigma^0(\theta, u_{10}, \varphi) = B_0(1 + B_1 cos(\varphi) + B_2 cos(2\varphi))^{1.6} \tag{4.6}$$

where u_{10} is the wind speed at 10 m height and φ is the angle between the wind vector and the radar look vector. B_0, B_1 and B_2 are the model parameters. They also depend on θ and u_{10}. B_1 and B_2 relate to upwind/downwind and upwind/crosswind amplitudes, respectively.

There is a number of models of these type, we mention only a few here. Well known examples are CMOD type models in C-Band, namely CMOD-IFR2 (Bentamy et al., 1999), CMOD5 (Hersbach, Stoffelen, and Haan, 2007) and CMOD5.n (Hersbach, 2010) and the X-Band models, XMOD1 (Ren et al., 2012) and XMOD2 (Li and Lehner, 2014). The latter was used for wind speed retrieval in paper A, for deriving the tilt modulation (discussed later) in paper B and as a forward model in the Bayesian retrieval method proposed in paper C.

How SAR images waves and currents: modulation transfer function

As mentioned in previous sections, SAR measures mainly the backscattered power from the Bragg waves. In principle, it does not directly image the long waves, i.e. $\lambda_w \geq n \ \lambda_B$, where n is between 3 and 10. Long waves are detected, indirectly, by SAR (Alpers, Ross, and Rufenach, 1981), based on four mechanisms: tilt modulation, hydrodynamic modulation, range bunching and velocity bunching (Alpers, Ross, and Rufenach, 1981; Hasselmann et al., 1985; Ouchi, 1988).

A complete description of these mechanisms is beyond the scope of this thesis (for more details see e.g. Robinson, 2004), but here follows a brief description. Tilt modulation is the modification of the local incidence angle by the slopes of the long waves. Hydrodynamic modulation is due to the straining and stretching of the Bragg waves by the orbital velocities of the long waves. Range bunching, called foreshortening and layover in SAR land imaging, is due the fact that the position of a scatterer in a SAR image in the range direction depends on its height. Ocean waves will change non uniformly the height of the scatterers along the wave profile. Thus scatterers on the peaks and trough will be displaced and imaged closer to each other, i.e. bunching. Velocity bunching is due to the fact that the position of a scatterer in a SAR image in the azimuth direction is based on the Doppler shift, hence on the scatterer's relative velocity. Thus, scatterers (roughness patches) riding long waves will be non-uniformly displaced in azimuth direction, because the wave will give different patches, different velocities (positive and negative).

Tilt, hydrodynamic and range bunching yield maximum modulation for waves traveling in the range direction and vanish for waves traveling in the azimuth direction. On the other hand, velocity bunching is maximum and vanishes for waves traveling in the azimuth and range direction, respectively. The four modulation mechanisms are illustrated schematically in Figure 4.2. Note that the illustration assumes linear modulation which is valid for waves of small amplitude and small slope. It can be observed from Figure 4.2, that tilt and range bunching yield an enhanced backscatter at the wave front facing the radar and weaker backscatter at the wave front looking away from the radar, independently of the wave propagation direction. The hydrodynamic modulation yields an enhanced and weaker backscatter at the leading and trailing front of the wave, respectively, hence the dependence on the wave propagation direction. This is actually the only mechanism allowing the radar to distinguish between the upwind and downwind direction. Velocity bunching also depends on the wave propagation direction, it thus yields a backscatter enhancement at the peaks or the troughs of the wave.

The surface currents are also imaged by SAR based on the hydrodynamic modulation mechanism (Kudryavtsev et al., 2005; Johannessen et al., 2005). In fact, SAR images the current gradient, i.e. a constant current affects the mean backscatter but it does not modulate the backscatter. Similar to the long waves, spatial variations of currents generate convergence and divergence zones of the surface roughness hence the modulation of the backscatter. The current modulation is usually manifested as a bright line of enhanced backscatter (Johannessen et al., 1991). The amplitude of this modulation depends on the relative direction between the wave propagation direction and the current. Finally, internal waves (Alpers, 1985) and sea floor topography (Alpers and Hennings, 1984) are also imaged by the same mechanism (hydrodynamic modulation). It is worth noting that other authors, (e.g. Kudryavtsev, Mastenbroek, and Makin, 1997) investigated the variation of the wind surface stress over long waves which also modulates the short wind-generated waves and the effect of breaking waves.

4.3 Doppler spectrum

The Doppler spectrum of the ocean surface, in the presence of Bragg waves and absence of long waves and currents, measured by a stationary radar will be dominated by two peaks at the frequencies ($\pm f_B$) corresponding to Bragg waves moving toward and away from the radar (Crombie, 1955; Barrick, 1972). A patch (facet) of Bragg waves propagating with the phase speed is also advected by the orbital velocities of long waves and by currents. This affects the Doppler spectrum measured by the radar as follows.

The orbital velocities of the long waves broaden the spectral lines at the Bragg frequencies (Plant and Keller, 1990; Romeiser and Thompson, 2000). The distribution of the orbital velocities is assumed to be zero-mean Gaussian. The correlation between the modulation of the backscatter (due to wave slopes) and the facet velocity (due to wave orbital motion) yields a net velocity in the direction of the propagation of the wave (Thompson, 1989; Romeiser and Thompson, 2000; Chapron, Collard, and Ardhuin, 2005; Johannessen et al., 2008). This consequently yields a shift of the Doppler spectrum. For instance, a facet tilted toward the radar, riding a long wave propagating away from the radar, will have a higher backscatter (than a facet tilted away) and negative velocity. Thus the backscatter-weighted mean velocity yields a shift of the Doppler spectrum toward negative frequencies in this case. This is illustrated schematically in Figure 4.3. Finally, the whole Doppler spectrum is shifted due to the presence of a mean current depending on its magnitude and direction.

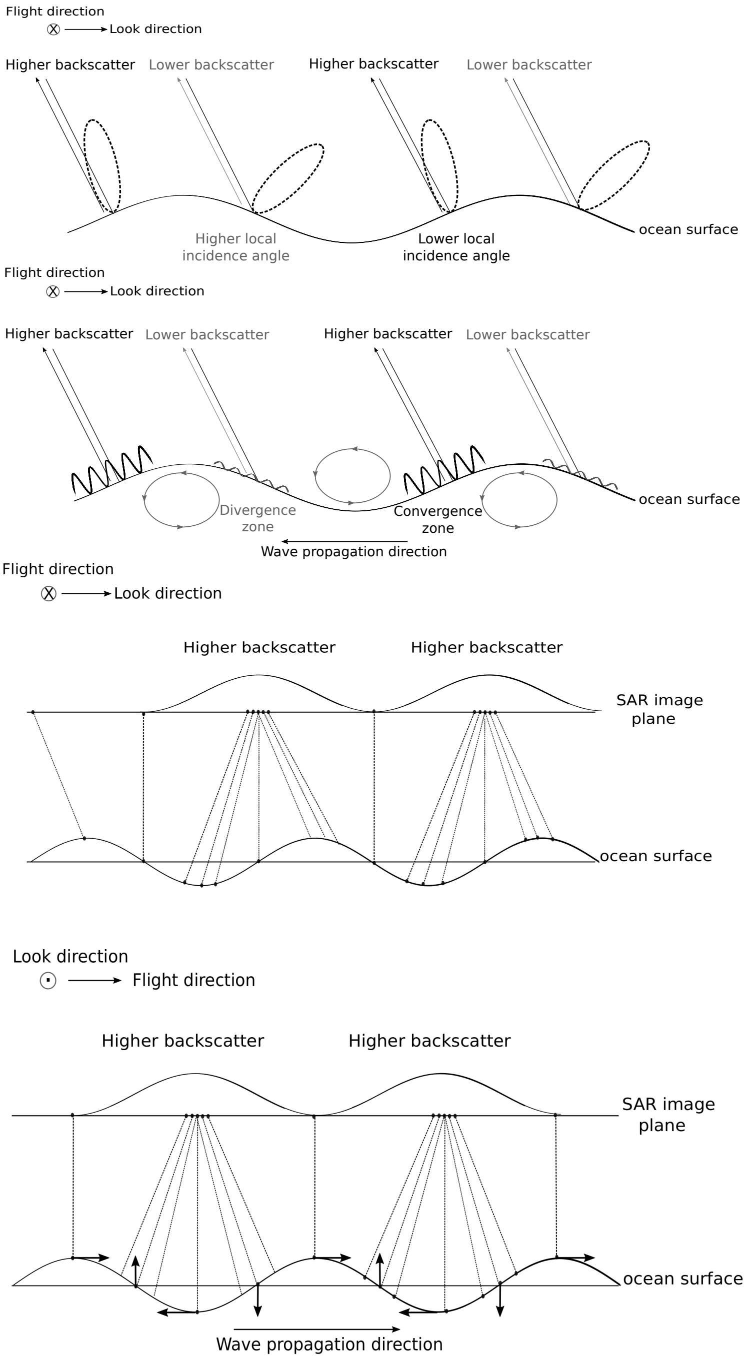

Figure 4.2. *SAR imaging of ocean surface waves: Tilt modulation (first row), hydrodynamic modulation (second row), range bunching (third row) and velocity bunching (fourth row).*

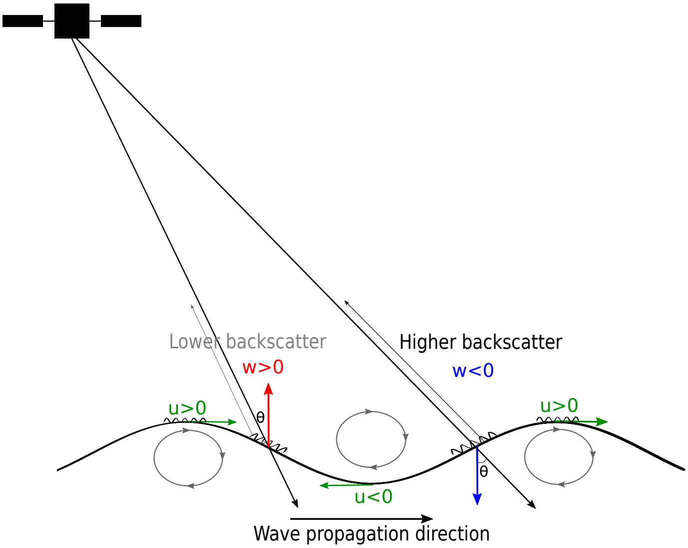

Figure 4.3. *Doppler shift due to power-weighted mean velocity. The wave is propagating in the range direction. u and w are the horizontal and vertical components of the wave orbital velocity.*

The Doppler spectrum S_D of a random ocean surface can be modeled as a mixture of two Gaussian-shaped power spectra (Romeiser and Thompson, 2000).

$$S_D(f) = \frac{\langle \sigma^0_+ \rangle}{\sqrt{2\pi}\sigma_D} e^{-\frac{(f-\langle f_{D+} \rangle)^2}{2\sigma_D^2}} + \frac{\langle \sigma^0_- \rangle}{\sqrt{2\pi}\sigma_D} e^{-\frac{(f-\langle f_{D-} \rangle)^2}{2\sigma_D^2}} \tag{4.7}$$

where $\pm$ refer to advancing and receding Bragg waves. The two power spectra are centered around $\langle f_{D\pm} \rangle$ which includes a first term due to the Bragg phase speed, a second term due to the backscatter-weighted mean Doppler shift (due to backscatter-velocity correlation discussed above) and a third term due to surface current. The amplitudes of the two spectra are defined by the mean backscatter associated with the two Bragg frequencies. The ratio between the backscatter associated with the advancing and receding Bragg waves is given by the directional wave spectrum. The width of the two spectra (σ_D^2) is determined primarily by the variance of the orbital velocities of the long waves, see (Thompson, 1989; Romeiser and Thompson, 2000).

If we assume that the backscatter modulation and correlation is the same for the advancing and receding Bragg waves, then the Doppler centroid (of the mixture) can be directly calculated as

$$\langle f_D \rangle = \langle f_B \rangle + \langle f_w \rangle + f_c \tag{4.8}$$

The Bragg term is given by

$$\langle f_B \rangle = \frac{k_e}{\pi} \frac{\Psi(k_B, 0) - \Psi(k_B, \pi)}{\Psi(k_B, 0) + \Psi(k_B, \pi)} c_B \sin\theta \tag{4.9}$$

where c_B is the Bragg phase speed. For TanDEM-X and Sentinel-1, the Bragg wave, at $\theta = 35^o$, will have a phase speed c_B of $\sim 0.20\ m/s$ and $\sim 0.27\ m/s$, respectively.

The term due to correlation is the average of the radial velocity of the scatterers weighted by the local σ^0 (Romeiser and Thompson, 2000; Chapron, Collard, and Ardhuin, 2005; Johannessen et al., 2008)

$$\langle f_w \rangle = \frac{k_e}{\pi} \frac{\langle u_r \, \sigma^0 \rangle}{\langle \sigma^0 \rangle} \tag{4.10}$$

where $u_r (= -w \cos\theta + u \sin\theta \cos\varphi)$ is the line-of-sight projection of the wave orbital velocity and u and w are its horizontal and vertical components.

The ocean current term is given by

$$f_c = \frac{k_e}{\pi} u_c \sin\theta \cos\varphi_c$$

where u_c is the horizontal current velocity and φ_c is the azimuth angle between the current vector and the radar line-of-sight.

For the Doppler spectrum measured by the (moving) SAR, the platform motion and antenna pattern must be taken into account. The Doppler spectrum above (equation 4.7) must be convolved with the Doppler spectrum due the platform motion and antenna pattern. Usually, the system has a larger Doppler bandwidth than the ocean spectrum. Moreover, the separation between the two Bragg lines at C- and X-band is below 30 Hz (depending on incidence angle). The SAR Doppler bandwidth is typically a few hundred Hz to a few kHz. Thus the total Doppler spectrum shape will be dominated by the antenna azimuth radiation pattern, i.e. Gaussian-like shape. Generally, the two Bragg lines are not distinguishable at C- and X-band. The total DC is the sum of the SAR system (geometric) DC (equation 3.3) and the stationary-radar ocean spectrum DC $\langle f_D \rangle$ (equation 4.8).

Experiments, (e.g. Plant, 1997, paper B), show that the Bragg/composite surface model predicts a Doppler shift difference between HH and VV polarizations that is much larger than the observed difference. This discrepancy between the model and data has led various investigators to find explanations in the non-Bragg scattering from bound waves (e.g. Plant, 1997) and breaking waves (e.g. Smith, Poulter, and McGregor, 1996).

Empirical models

Similar to backscatter models, these are called geophysical model functions. Such GMFs are built using a large number of collocated radar-estimated Doppler shifts and wind data provided by in-situ observations or NWP models. Thus they are also frequency and polarization dependent. We limit this discussion to C and X-band GMFs which are relevant to this work. In contrast to backscatter models, the development of empirical Doppler models is in its early stage. Thus only few models exist. To our knowledge, the only available GMF that covers the two polarizations (HH and VV), a large range of incidence angles, wind speeds and directions is called CDOP, which was built from a large global dataset provided by the C-band SAR ENVISAT/ASAR (Mouche et al., 2012). This GMF was used for the correction of the wave-induced Doppler shift in paper A, for comparison to the empirical GMF developed in paper B and used as a forward model in the Bayesian retrieval method proposed in paper C.

Inversion methods

5

This chapter assumes a single beam and single polarization SAR.

5.1 Direct method

This method allows only the retrieval of the wind speed provided that wind direction is known and the retrieval of the radial current provided that wind speed and direction are known. In some cases, the wind direction can be extracted from SAR images.

5.1.1 Wind retrieval

Wind speed

Wind speed retrieval is an inverse problem. Like any inverse problem, a forward model is required. The forward models used in wind retrieval are generally empirical (GMF). They relate the wind speed and direction to σ^0 as

$$\sigma^0 = GMF_{\sigma^0}(\theta, u_{10}, \varphi, f, pol) \tag{5.1}$$

where u_{10} is the wind speed at 10 m height, φ is the angle between the wind direction and the antenna beam, θ is the incidence angle, f is the frequency and pol is the polarization (VV or HH). Figure 5.1 depicts the variation of the XMOD2 GMF with incidence angle, wind speed and direction. Observe that the backscatter is particularly strongly dependent on wind speed, which makes SAR a good sensor of wind speed. The wind direction is usually obtained from another source, typically from a numerical weather prediction model or in-situ observations. It can also be extracted from SAR images (see below).

The least-squares solution to the inversion problem is finding the wind speed that minimizes the squared difference between the measured and simulated backscatter, i.e. minimize the following cost function

$$J(V) = \sum_i (\sigma^0_{meas_i} - GMF_{\sigma^0}(\theta, u_{10}, \varphi, f, pol))^2 \tag{5.2}$$

where σ^0_{meas} is the measured backscatter. The sum is ideally an ensemble average if different measurements are available or a spatial average if homogeneity can be assumed.

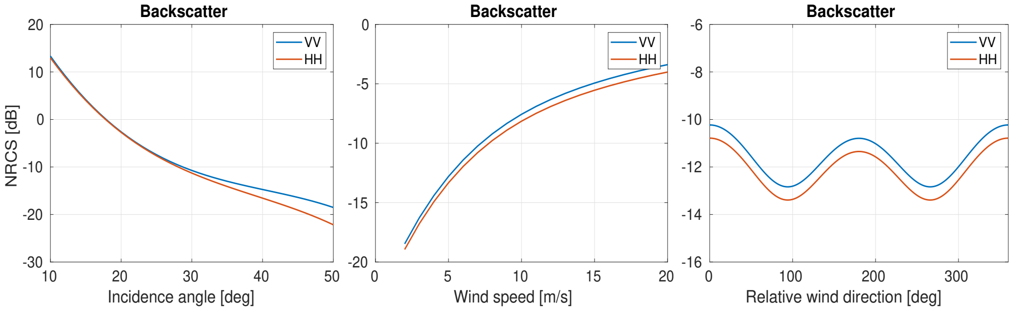

Figure 5.1. *Backscatter computed using the XMOD2 GMF, for VV and HH polarization, left: as a function of incidence angle (u_{10}=7 m/s, φ=0), middle: wind speed (θ=30°, φ=0) and right: relative wind direction (u_{10}=7m/s, θ=30°).*

Wind direction

In the previous section, it is assumed that the wind direction is provided by an external source such as an atmospheric model. It is also possible, in some cases, to extract the wind direction directly from SAR images (Wackerman et al., 1996; Koch, 2004). The underlying assumption is that Langmuir circulation cells in the surface layer and atmospheric roll vortices induce convergence/divergence bands closely parallel to the wind direction (Gerling, 1986; Alpers and Brummer, 1994). This wind direction extraction is based on the detection of these features (convergence/divergence bands) and their alignment. This is achieved by edge detection techniques in the spatial domain such as Local Gradient (LG) technique (Wackerman et al., 1996; Koch, 2004; Carvajal, Eriksson, and Ulander, 2014) or in the spectral domain using Fourier transform (Wackerman et al., 1996).

5.1.2 Radial current retrieval

As discussed in section 4.2, assuming that the geometric DC is removed, even in the absence of ocean currents the SAR Doppler centroid will contain a contribution from wave motion. Moreover, this contribution is often larger than the proper current (water mass transport) contribution (see paper 1 for more details). Thus, in order to retrieve the ocean current, this wave contribution needs to be estimated and removed. This can be achieved by using a Doppler model. This model, ideally, simulates what Doppler shift the SAR would measure from wave motion for a given wind speed and direction in the absence of currents.

Theoretical models were first developed, e.g. M4S (by Romeiser and Thompson, 2000) and DopRim (by Johannessen et al., 2008). Later, an empirical model, called CDOP, was developed by (Mouche et al., 2012) for C-band. Similar to wind retrieval, empirical models (GMFs) can be used for current retrieval. The CDOP GMF has the form

$$f_{DOP} = GMF_{Dop}(\theta, u_{10}, \varphi, f, pol) \tag{5.3}$$

where the arguments of the Doppler GMF have the same definitions as the arguments of the wind GMF in equation 5.1.

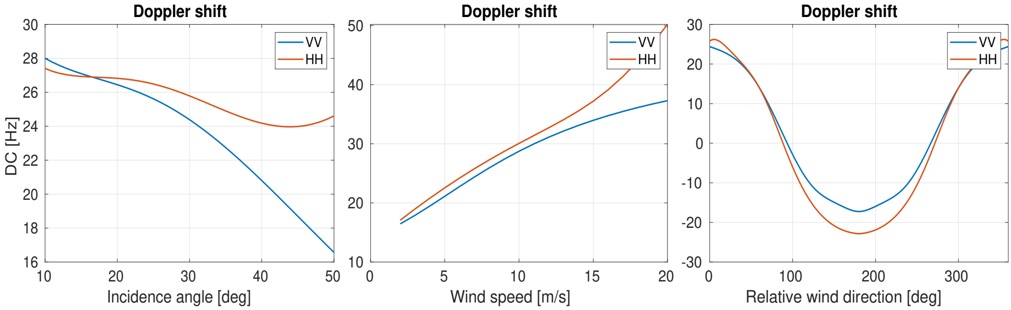

Figure 5.2. *Doppler frequency shift computed using the CDOP GMF, for VV and HH polarization, , left: as a function of incidence angle (u_{10}=7 m/s, φ=0), middle: wind speed (θ=30°, φ=0) and right: relative wind direction (u_{10}=7m/s, θ=30°).*

The variation of the CDOP GMF with incidence angle, wind speed and direction is depicted in Figure 5.2. Observe that the DC is particularly strongly dependent on the wind direction.

The simulated Doppler shift is subtracted from the measured Doppler shift as

$$f_c = f_{D_{meas}} - GMF_{Dop}(\theta, u_{10}, \varphi, f, pol) \tag{5.4}$$

Note that this does not take into account the wave-current interaction which consists of the modulation of the wave spectrum by the currents gradient (Romeiser and Thompson, 2000; Johannessen et al., 2005).

5.2 Bayesian method

The Bayesian inversion is based on the maximum a posteriori estimation method (MAP), also called optimal estimation method (OEM) (Rodgers, 2000). In the data assimilation (DA) framework, it is commonly referred to as 2D variational method (2D-VAR). In short, the principle of the Bayesian approach is combining a priori information with the measurements, referred to as background and observations in the DA framework, assuming that all sources of information contain errors and these errors are well characterized. The solution **x** that maximizes the posterior probability p(**x**/**y**) is sought

$$P(\mathbf{x}/\mathbf{y}) \propto P(\mathbf{y}/\mathbf{x})P(\mathbf{x}) \tag{5.5}$$

where $P(\mathbf{x}/\mathbf{y})$, $P(\mathbf{y}/\mathbf{x})$ and $P(\mathbf{x})$ are the posterior, the likelihood and the prior distributions. **x** and **y** are the state (or analysis in DA framework) and the observation vectors, respectively.

MAP is equivalent to minimizing a cost function given by (Lorenc, 1988)

$$J(\mathbf{x}) = J_B(\mathbf{x}) + J_O(\mathbf{x}) \tag{5.6}$$

where $J_B(\mathbf{x})$ is the background term describing the deviation between the state variable and the background and $J_O(\mathbf{x})$ is the observation term describing the deviation between the observation and the state variable mapped into the observation space using a forward model.

Assuming **x** and **y** both have Gaussian distributions, the cost function reads

$$J(\mathbf{x}) = \frac{1}{2}(\mathbf{x} - \mathbf{x}_B)^T \mathbf{B}^{-1}(\mathbf{x} - \mathbf{x}_B) + \frac{1}{2}(\mathbf{y} - \mathbf{F}(\mathbf{x}))^T \mathbf{R}^{-1}(\mathbf{y} - \mathbf{F}(\mathbf{x})) \tag{5.7}$$

where $\mathbf{x}_B$ is the background vector, also called the a priori, **B** and **R** are the covariance matrices of the background and observation, respectively.

The observation **y** and the state vector **x** are related by the forward model **F** as follows

$$\mathbf{y} = \mathbf{F}(\mathbf{x}, p) + \epsilon_o \tag{5.8}$$

where $\epsilon_o = \epsilon_{mod} + \epsilon_{rep} + \epsilon_{inst}$ is the observation error, which is composed of the forward model error, representation error and instrument error respectively. ϵ_{mod} includes errors in the model physics and parameters, ϵ_{rep} reflects the spatial and temporal mismatch between the measurements and the model, ϵ_{inst} reflects the instrument and processing errors. p groups all the model parameters.

Equation 5.7 is solved iteratively using an optimization algorithm. The algorithm is initialized with realistic values of **x**, typically $\mathbf{x}_B$ is chosen as the initial value. The algorithm updates **x** iteratively and re-calculates J at each iteration until it does not decrease significantly, i.e. the difference between consecutive iterations is lower than a given threshold. Optimization algorithms mainly differ in the way they choose the test value for **x**. The basic idea is that **x** is chosen from a set of possible values (if the algorithm allows constraints) and such that it makes J smaller than the previous iteration. Most algorithms achieve this by following the gradient or the Hessian of the cost function (Rodgers, 2000).

In the context of wind and current retrieval from SAR, **x** is the wind and current vector, i.e. the retrievals, and **y** is the measured NRCS (σ^0) and Doppler frequency shift (DC). $\mathbf{x}_B$ is the a priori value of the wind and current, which are usually obtained from an atmospheric and oceanic model, respectively. The forward model can be theoretical or empirical. Empirical GMFs are more efficient in terms of computation speed. This method is used in paper C to retrieve the total wind and current vector.

6

Summary of Appended Papers

6.1 Paper A: Measurements of Sea Surface Currents in the Baltic Sea Region using Spaceborne Along-Track InSAR

The main challenging problems in ocean current retrieval from along-track interferometric synthetic aperture radar are phase calibration and the estimation and removal of the wave contribution. In this paper, a method based on differential interferometric SAR (DInSAR) technique for correcting the phase offset and its range variation is proposed. The method uses a digital elevation model (DEM) to simulate the topographic phase. The simulated topographic phase is subtracted from the total phase. A 2D polynomial surface is fitted, using land pixels, and removed from the residual phase. The wave contribution (also called wave bias) is estimated using two different Doppler models and two different wind sources. Of the two Doppler models, one is theoretical (M4S) and one is empirical (CDOP). The two wind sources used for wave correction are provided by an atmospheric model (HIRLAM) and the wind speed retrieved from the calibrated SAR backscatter using an empirical geophysical model function (XMOD2). We analyzed four TanDEM-X acquisitions over the Öresund channel, which is an important transition area between the the Baltic Sea and the Kattegat Sea. The retrieved currents are compared to a regional ocean circulation model (HBM) provided by the Danish meteorological institute (DMI). It is shown that by applying the proposed phase correction and wave bias removal, a good agreement in spatial variation and current direction is achieved. The residual bias, between the ocean model and the current retrievals, varies between 0.013 and 0.3 m/s depending on the Doppler model and wind source used for wave correction. It is found that current retrieval is highly sensitive to errors in the wind vectors and the used Doppler models. The paper results show that using SAR as a source of wind speed reduces the bias and root-mean-squared-error of the retrieved currents by 20% and 15%, respectively. The paper also shows that the correction using the empirical Doppler model yields a better agreement with the ocean model than using the theoretical Doppler model. Finally, it was found that the retrieved currents were qualitatively in agreement with the in-situ sea level measurements at the two ends of the channel.

Contribution to paper: I processed the data, produced the analysis results and prepared the manuscript. Interpretation of the results was done together with the co-authors.

6.2 Paper B: Empirical Relationship between the Doppler Centroid derived from X-Band Spaceborne InSAR Data and Wind Vectors

As was found in paper A, ocean surface current retrieval from SAR data is very sensitive to the estimation of the wave-induced Doppler centroid (DC), i.e. using different Doppler models for the wave contribution removal yields different current retrievals. This paper demonstrates empirically the relationship between the DC derived from the X-band InSAR (TanDEM-X) data and the ocean surface wind and waves, for both VV and HH polarizations. First, we have shown that theoretical Doppler models are very sensitive to the parameterization of the modulation transfer function (MTF). Second, in order to analyze the Doppler-wind relationship, over 300 TanDEM-X image pairs were processed. It is found that the general characteristics of the estimated DC follow the theoretically expected variation with incidence angle, wind speed and wind direction. The estimated average DC from each image pair is matched with a wind vector provided by ERA5 reanalysis data. An empirical geophysical model function (GMF) is fitted to the estimated DC and the fitted GMF is compared to the empirical C-band model CDOP, the theoretical model M4S, the X-band Wavemill proof-of-concept dataset and the Ka-band semi-empirical model KaDOP. Our GMF is in a good agreement (within 0.2 m/s) with these models and datasets. It is found that the wave-induced Doppler velocity contributes to the total Doppler velocity with about 15$\%$ of the relative wind speed. This is much larger than the sum of the contributions from the Bragg waves ($\sim$0.2 m/s) and the wind drift ($\sim$3$\%$ of the wind speed). This indicates a significant (dominant) contribution of the long waves to the SAR DC. Moreover, analysis of dual-polarization data shows that the backscatter polarization ratio (PR=$\sigma^0_{VV}/\sigma^0_{HH}$) and the DC polarization difference (PD=$|DC_{VV}| - |DC_{HH}|$) are systematically larger than 1 and smaller than 0, respectively, and both increase in magnitude with incidence angle. The estimated PR and PD are compared to other theoretical and empirical models. The Bragg scattering theory-based (pure Bragg and composite surface) models overestimate both PR and PD, suggesting that other scattering mechanisms, e.g. wave breaking, are involved. A semi-empirical Doppler model based on a MTF estimated from an empirical backscatter GMF is proposed. It is shown that this model is more consistent, in terms of PR and PD, with both backscatter and Doppler data than theory-based models. This study motivates a further development and improvement of SAR Doppler GMFs. These GMFs are required for operational ocean current retrieval from SAR data. To understand and resolve the discrepancy between the different models and datasets, more SAR Doppler data are needed.

Contribution to paper: I processed the data, implemented the Doppler model, produced the analysis results and prepared the manuscript. Interpretation of the results was done together with the co-authors.

6.3 Paper C: Joint Retrieval of Ocean Surface Wind and Current Vectors from Satellite SAR Data using a Bayesian Inversion Method

In paper A, the ocean current retrieval was based on the direct method with the limitation to the radial component only. Paper A showed that current retrievals are directly affected by uncertainties in wind vectors and Doppler models used for wave correction. In paper B, it was shown that the uncertainties in the existing Doppler models are not yet resolved. In this paper we attempt the retrieval of the total current and wind vectors using a priori knowledge. A method is presented for joint retrieval of the ocean surface wind and current vectors using the backscatter and the Doppler frequency shift measured by spaceborne single-beam, single-polarization synthetic aperture radar. The retrieval method is based on the Bayesian approach with the a priori information provided by atmospheric and oceanic numerical models for surface wind and currents, respectively. The background winds and currents are provided by the UERRA reanalysis dataset and the NEMO-Nordic ocean circulation model, respectively. The Doppler frequency shift can, in principle, be estimated using the Doppler centroid anomaly analysis (DCA) or the along-track interferometric (ATI) technique. In this paper, the Doppler frequency shift is estimated from TanDEM-X data using the ATI technique, but the retrieval method is applicable to both DCA and ATI. The retrieval results are compared against in-situ measurements along the Swedish west coast. It is found that the wind retrieval reduces the atmospheric model bias compared to in-situ measurements by about 1 m/s and 10° for wind speed and direction, respectively. The ocean model bias compared to in-situ measurements is reduced by about 0.1 m/s and 35° for current speed and direction, respectively. It is shown that blending SAR data with model data is particularly useful in complex situations such as atmospheric and oceanic fronts. This is demonstrated through two case studies, an atmospheric front in the Skagerrak Sea and an oceanic front along the Swedish west coast. For the atmospheric front, the SAR-derived wind speed gradient is much larger and sharper than the model gradient. Moreover, the SAR-observed wind front is in close agreement with the front derived with the C-band scatterometer ASCAT. The retrieved front is a smoothed version of the observed one, but is still sharper than the front provided by the atmospheric model. For the oceanic front, the sea surface temperature (SST) gradient induced by the current is manifested in the SAR-observed wind speed. The SST-induced wind speed gradient is in close agreement with the SST measured by the Metop-A/AVHRR radiometer. Moreover, the retrieval successfully introduces the small scale circulation features, e.g. current meandering, detected by SAR and preserves the large scale circulation imposed by the models.

Contribution to paper: I processed the data, implemented the retrieval algorithm, produced the analysis results and prepared the manuscript. Interpretation of the results was done together with the co-authors.

6.4 Paper D: Wind Direction Ambiguity Removal using Along-Track INSAR: A Case Study

As mentioned earlier, both the wind and current retrieval from SAR data require the knowledge of the wind direction. This wind direction information is usually provided by NWP models or in-situ data. A few methods have been proposed to extract the wind direction from SAR images. The main limitation of these methods is the 180° ambiguity in the direction. Usually, an external source of wind direction, e.g. a NWP, is used to remove this ambiguity. From previous experience, it was noticed that the SAR Doppler shift is dominated by the wind. In this study, we wanted to exploit the Along-track Interferometric SAR (ATI-SAR) phase to demonstrate its usefulness to tackle the wind direction ambiguity problem. A method is proposed to remove the wind direction ambiguity using the ATI-SAR phase information. This is based on the fact that the interferometric phase is related to the sea surface wind-waves propagation direction. That is to say the ATI phase is positive and negative in upwind and downwind, respectively. This effect is used to assist the wind extraction algorithm to select the most plausible direction. The results show a very good agreement with atmospheric models and visual investigation of wind shadow.

Contribution to paper: I processed the data, produced the analysis results and prepared the manuscript. Interpretation of the results was done together with the co-authors.

6.5 Paper E: Using Sentinel-1 Ocean Data for Mapping Sea Surface Currents Along the Southern Norwegian Coast

All previous studies were based on the ATI-SAR TanDEM-X data. Note that the analysis in paper B and the retrieval algorithms in papers A and C are applicable to Doppler shift independently of its source (ATI and DCA). However, different imaging modes employed by TanDEM-X, e.g. stripmap and Sentinel-1, e.g. TOPSAR, might affect the Doppler data differently. In this paper, the capability of Sentinel-1 data (produced using the DCA technique) to map ocean surface currents in the Skagerrak Sea, with a focus on the Norwegian Coastal Current (NCC), is investigated. Post-processing methods for removal of artifacts in the data and improvement of the geophysical interpretation are suggested. Scalloping is one major artifact that significantly degrades the quality of the velocity maps. Two methods, in spatial and spectral domain, for correcting this effect are proposed. It is also found that the radial velocity provided in the Sentinel-1 ocean data is biased, hence land is used as a reference to correct for the absolute and inter-beam bias. The wind-wave contribution is estimated using the empirical model CDOP and removed from the total radial velocity. Finally, the retrieved (corrected) velocity is compared to a regional ocean circulation model (ROMS). It is shown that there is a good agreement between the ocean model and the retrieved velocity with values of $\sim$0.8 m/s in the core of the NCC.

Contribution to paper: I processed the data, produced the analysis results and prepared the manuscript. Interpretation of the results was done together with the co-authors.

7

Conclusions and Outlook

7.1 Conclusions

The main outcomes of this thesis from the analysis of the backscatter and the Doppler frequency shift derived from satellite-borne SAR (TanDEM-X and Sentinel-1) are the following

- The achievable precision of Doppler shift, given some averaging, satisfies the requirement ($\sigma_{f_D} \leq 5$ Hz) for current retrieval, but accuracy requires calibration. The best calibration reference is land. In case of systems such as TanDEM-X, the calibration requires a DEM. (Papers A and C)
- The contribution of waves to the SAR Doppler shift is often dominant over the current contribution. This wave contribution can be simulated using existing Doppler models, provided wind vectors are known, and removed from the measured Doppler shift. (Papers A and B)
- Ocean current retrieval is sensitive to the used Doppler model and to errors in the wind vectors used to estimate the wind-wave contribution. Using wind speed retrieved from SAR, combined with an empirical Doppler model, improves the simulation significantly. (Paper A)
- The SAR-derived Doppler shift can be used to remove the wind direction ambiguity extracted from SAR. This ambiguity is a problematic limitation that hinders SAR wind vector retrieval. (Paper D)
- Correlation between the ocean surface wind vectors and the Doppler shift derived from TanDEM-X ATI data was demonstrated empirically for VV and H polarizations for the first time, to our knowledge. (Paper B)
- The proposed semi-empirical Doppler model based on an empirical MTF derived from a backscatter GMF provides better agreement with data, in terms of polarization ratio ($\sigma^0_{VV}/\sigma^0_{HH}$) and polarization difference ($f_{D_{VV}}$-$f_{D_{HH}}$), than pure theoretical models. (Paper B)
- The feasibility of retrieval of the total wind and current vector from spaceborne single-polarization single-beam SAR backscatter and Doppler shift using a Bayesian inversion approach is, to our knowledge, demonstrated for the first time. (Paper C)
- The radial velocity provided by the Sentinel-1 OCN product suffers from a few artifacts. Scalloping, inter-swath bias and the absolute bias are the main issues. Post-processing methods can be used to mitigate these artifacts and improve the utilization of these data. (Paper E)

7.2 Outlook

The work presented in this thesis will continue. Here are a few tasks that we hope to perform over the next years:

- Experimental campaign at the southern coast of Norway in collaboration with the Norwegian meteorological institute. Drifters, HF radars will be used to validate SAR data (Sentinel-1 and TanDEM-X if available).
- Comparison of the currents retrieved from existing SAR data against coastal HF radars, when temporal and spatial collocation with satellite data is available.
- Development of an X-band empirical Doppler model, if more X-Band ATI data are available, e.g. additional TanDEM-X science campaigns.
- Improvement of the proposed Doppler model (Paper B), e.g. estimating wind and wave parameters directly from SAR data and taking into account wave breaking.
- Improvement of the existing backscatter GMF, e.g. taking into account the sea surface temperature, air-sea temperature difference and current velocity.
- Set up a high resolution ($\leq$300 m) ocean circulation model for a limited area in the Baltic Sea region, to test the effect of different parameterizations, e.g. wind forcing, initial condition, hydrostatic assumption, high resolution bathymetry.
- Set up a high resolution ($\leq$300 m) ocean wave model for a limited area in the Baltic Sea region, for assessment of the integral wave parameters derived from SAR data, assessment of the existing wave spectra models and estimation of the Stokes drift.
- Application of the retrieval methods presented in this thesis to future concepts/missions such as SEASTAR (Gommenginger et al., 2019), STEROID (Dekker et al., 2018) and TanDEM-L (Moreira et al., 2011).

References

Alpers, W. (1985). Theory of radar imaging of internal waves. *Nature Letters*, vol. 314, 245–247.

Alpers, W. and Brummer, B. (1994). Atmospheric boundary layer rolls observed by the synthetic aperture radar aboard the ERS-1 satellite. *Journal of Geophysical Research*, vol. 99, no. C6, pp. 12613–12621.

Alpers, W., Ross, D. B., and Rufenach, C. L. (1981). On the detectability of ocean surface waves by real and synthetic aperture radar. *Journal of Geophysical Research: Oceans*, vol. 86, no. C7, pp. 6481–6498.

Alpers, W. and Hennings, I. (1984). A theory of the imaging mechanism of underwater bottom topography by real and synthetic aperture radar. *Journal of Geophysical Research: Oceans*, vol. 89, no. C6, pp. 10529–10546.

Apel, J. R. (1987). *Principles of ocean physics*. Vol. 38. International geophysics series. Academic press.

Ardhuin, F. et al. (2009). Observation and estimation of Lagrangian, Stokes, and Eulerian currents induced by wind and waves at the sea surface. *Journal of Physical Oceanography*, vol. 39, no. 11, pp. 2820–2838.

Ardhuin, F. et al. (2018). Measuring currents, ice drift, and waves from space: the sea surface kinematics multiscale monitoring (SKIM) concept. *Ocean Science*, vol. 14, no. 3, pp. 337–354.

BACCII author team (2015). *Second assessment of climate change for the baltic sea basin*. Springer, Cham.

Bamler, R. and Hartl, P. (1998). Synthetic aperture radar interferometry. *Inverse Problems*, vol. 14, no. 4, R1.

Barrick, D. (1968). Rough surface scattering based on the specular point theory. *IEEE Transactions on Antennas and Propagation*, vol. 16, no. 4, pp. 449–454.

Barrick, D. (1972). First-order theory and analysis of MF/HF/VHF scatter from the sea. *IEEE Transactions on Antennas and Propagation*, vol. 20, no. 1, pp. 2–10.

Bass, F. et al. (1968). Very high frequency radiowave scattering by a disturbed sea surface part II: scattering from an actual sea surface. *IEEE Transactions on Antennas and Propagation*, vol. 16, no. 5, pp. 560–568.

Bentamy, A. et al. (1999). Ocean surface wind fields estimated from satellite active and passive microwave instruments. *IEEE Transactions on Geoscience and Remote Sensing*, vol. 37, no. 5, pp. 2469–2486.

Bentamy, A. et al. (2017). Homogenization of scatterometer wind retrievals. *International Journal of Climatology*, vol. 37, no. 2, pp. 870–889.

Bourassa, M. A., Vincent, D. G., and Wood, W. L. (May 1999). A flux parameterization including the effects of capillary waves and sea state. *Journal of the Atmospheric Sciences*, vol. 56, no. 9, pp. 1123–1139.

Bourras, D. et al. (2004). Response of the atmospheric boundary layer to a mesoscale oceanic eddy in the northeast atlantic. *Journal of Geophysical Research: Atmospheres*, vol. 109, no. D18.

Breivik, and Sætra, (2001). Real time assimilation of HF radar currents into a coastal ocean model. *Journal of Marine Systems*, vol. 28, no. 3, pp. 161 –182.

Carvajal, G. K., Eriksson, L. E. B., and Ulander, L. M. H. (2014). Retrieval and quality assessment of wind velocity vectors on the ocean with C-Band SAR. *IEEE Transactions on Geoscience and Remote Sensing*, vol. 52, no. 5, pp. 2519–2537.

Chapron, B., Collard, F., and Ardhuin, F. (2005). Direct measurements of ocean surface velocity from space: interpretation and validation. *Journal of Geophysical Research*, vol. 110.

Chelton, D. B. et al. (Apr. 2001). Observations of coupling between surface wind stress and sea surface temperature in the eastern tropical Pacific. *Journal of Climate*, vol. 14, no. 7, pp. 1479–1498.

Chelton, D. B. et al. (2004). Satellite measurements reveal persistent small-scale features in ocean winds. *Science*, vol. 303, no. 5660, pp. 978–983.

Chen, C., Shiotani, S., and Sasa, K. (2015). Effect of ocean currents on ship navigation in the east China sea. *Ocean Engineering*, vol. 104, pp. 283 –293.

Cox, C. and Munk, W. (1954). Measurement of the roughness of the sea surface from photographs of the sun's glitter. *Journal of the Optical Society of America*, vol. 44, no. 11, pp. 838–850.

Crombie, D. D. (1955). Doppler spectrum of sea echo at 13.56 Mc./s. *Nature*, vol. 175, 681–682.

Cumming, I. G. and Wong, F. H. (2005). *Digital processing of synthetic aperture radar data: algorithms and implementation*. Boston, London: Artech House Inc.

Dagestad, K.-F. et al. (2012). "Wind retrieval from synthetic aperture radar - an overview". Proceedings of SEASAR 2012.

Dawe, J. T. and Thompson, L. A. (2006). Effect of ocean surface currents on wind stress, heat flux, and wind power input to the ocean. *Geophysical Research Letters*, vol. 33, no. 9.

Dekker, P. L. et al. (2018). *Stereo thermo optically enhanced radar for Earth, ocean, ice, and land dynamics (STEREOID)*. Tech. rep. ESA Ref: CEE10/012. Delft University of Technology.

Donelan, M. A. and Pierson, W. J. (1987). Radar scattering and equilibrium ranges in wind-generated waves with application to scatterometry. *Journal of Geophysical Research: Oceans*, vol. 92, no. C5, pp. 4971–5029.

Döös, K., Meier, H. E., and Döscher, R. (2004). The Baltic haline conveyor belt or the overturning circulation and mixing in the Baltic. *Ambio*, vol. 33, no. 4-5.

Eineder, M., Fritz, T., and Mittermayer, J. (2008). *TerraSAR-X Ground Segment - Basic product specification document*. Tech. rep. DLR.

Ekman, V. (1905). On the influence of the Earth's rotation on ocean-currents. *Arkiv för Matematik, Astronomi och Fysik*, vol. 2, no. 11, pp. 1–52.

Elachi, C. and Brown, W. (1977). Models of radar imaging of the ocean surface waves. *IEEE Journal of Oceanic Engineering*, vol. 2, no. 1, pp. 84–95.

Elfouhaily, T. M. and Guérin, C.-A. (2004). A critical survey of approximate scattering wave theories from random rough surfaces. *Waves in Random Media*, vol. 14, R1 –R40.

Engen, G. et al. (1994). Directional wave spectra by inversion of ERS-1 synthetic aperture radar ocean imagery. *IEEE Transactions on Geoscience and Remote Sensing*, vol. 32, no. 2, pp. 340–352.

Fiedler, H. et al. (2005). Total zero Doppler steering - a new method for minimizing the Doppler centroid. *IEEE Geoscience and Remote Sensing Letters*, vol. 2, pp. 141–145.

Fung, A. (1994). *Microwave scattering and emission models and their applications*. Artech House remote sensing library. Artech House.

Gade, M. et al. (1998a). On the reduction of the radar backscatter by oceanic surface films: scatterometer measurements and their theoretical interpretation. *Remote Sensing of Environment*, vol. 66, no. 1, pp. 52 –70.

Gade, M. et al. (1998b). Wind-wave tank measurements of bound and freely propagating short gravity-capillary waves. *Journal of Geophysical Research: Oceans* , vol. 103, no. C10, pp. 21697–21709.

Gerling, T. W. (1986). Structure of the surface wind field from the Seasat SAR. *Journal of Geophysical Research*, vol. 91, no. C2, pp. 2308–2320.

Golbeck I., L. X.J.F.e. a. (2015). Uncertainty estimation for operational ocean forecast products—a multi-model ensemble for the North Sea and the Baltic Sea. *Ocean Dynamics* , vol. 65, 1603–1631.

Goldstein, R. and Zebker, H. (1987). Interferometric radar measurement of ocean surface currents. *Nature*, vol. 328, pp. 707–709.

Goldstein, R., Zebker, H., and Barnett, T. P. (1989). Remote sensing of ocean currents. *Science*, vol. 246 (4935), pp. 1282–1285.

Gommenginger, C. et al. (2019). SEASTAR: a mission to study ocean submesoscale dynamics and small-scale atmosphere-ocean processes in coastal, shelf and polar seas. *Frontiers in Marine Science*, vol. 6, no. 457, pp. 1–7.

Hansen, M. W. et al. (2011). Retrieval of sea surface range velocities from Envisat ASAR Doppler centroid measurements. *IEEE Transactions on Geoscience and Remote Sensing*, vol. 49, no. 10, pp. 3582–3592.

Hanssen, R. F. (2001). *Radar interferometry: data interpretation and error analysis*. 1st ed. Springer.

Hasager, C. B. et al. (2015). Offshore wind climatology based on synergetic use of Envisat ASAR, ASCAT and QuikSCAT. *Remote Sensing of Environment*, vol. 156, pp. 247 –263.

Hasselmann, K. and Hasselmann, S. (1991). On the nonlinear mapping of an ocean wave spectrum into a synthetic aperture radar image spectrum and its inversion. *Journal of Geophysical Research: Oceans*, vol. 96, no. C6, pp. 10713–10729.

Hasselmann, K. et al. (1985). Theory of synthetic aperture radar ocean imaging: A MARSEN view. *Journal of Geophysical Research: Oceans*, vol. 90, no. C3, pp. 4659–4686.

Hersbach, H., Stoffelen, A., and Haan, S. de (2007). An improved C-band scatterometer ocean geophysical model function: CMOD5. *Journal of Geophysical Research: Oceans*, vol. 112, no. C3.

Hersbach, H. (Apr. 2010). Comparison of C-Band scatterometer CMOD5.N equivalent neutral winds with ECMWF. *Journal of Atmospheric and Oceanic Technology*, vol. 27, no. 4, pp. 721–736.

Horstmann, J. and Koch, W. (2008). High resolution wind field retrieval from synthetic aperture radar: North Sea examples. *Remote sensing of the European seas*. Ed. by V. Barale and M. Gade. Dordrecht: Springer Netherlands, pp. 331–342.

Horstmann, J. et al. (2003). Global wind speed retrieval from SAR. *IEEE Transactions on Geoscience and Remote Sensing*, vol. 41, no. 10, pp. 2277–2286.

Isern-Fontanet, J. et al. (2017). Remote sensing of ocean surface currents: a review of what is being observed and what is being assimilated. *Nonlinear Processes in Geophysics*, vol. 24, no. 4, pp. 613–643.

Jenkins, A. D. (1987). Wind and wave induced currents in a rotating sea with depth-varying eddy viscosity. *Journal of Physical Oceanography*, vol. 17, no. 7, pp. 938–951.

Johannessen, J. A. et al. (1996). Coastal ocean fronts and eddies imaged with ERS-1 synthetic aperture radar. *Journal of Geophysical Research: Oceans*, vol. 101, no. C3, pp. 6651–6667.

Johannessen, J. A. et al. (2005). On radar imaging of current features: 2. mesoscale eddy and current front detection. *Journal of Geophysical Research: Oceans*, vol. 110, no. C7.

Johannessen, J. A. et al. (2008). Direct ocean surface velocity measurements from space: improved quantitative interpretation of Envisat ASAR observations. *Geophysical Research Letters*, vol. 35, no. 22.

Johannessen, J. A. et al. (1991). Synthetic aperture radar imaging of upper ocean circulation features and wind fronts. *Journal of Geophysical Research: Oceans*, vol. 96, no. C6, pp. 10411–10422.

Joseph, A. (2014). *Measuring ocean currents*. Ed. by A. Joseph. Boston: Elsevier, pp. 1 –49.

Koch, W. (2004). Directional analysis of SAR images aiming at wind direction. *IEEE Transactions on Geoscience and Remote Sensing*, vol. 42, no. 4, pp. 702–710.

Krieger, G. et al. (2007). TanDEM-X: a satellite formation for high-resolution SAR interferometry. *IEEE Transactions on Geoscience and Remote Sensing*, vol. 45, no. 11, pp. 3317–3341.

Kudryavtsev, V. et al. (2005). On radar imaging of current features: 1. model and comparison with observations. *Journal of Geophysical Research: Oceans*, vol. 110, no. C7.

Kudryavtsev, V. et al. (2003). A semiempirical model of the normalized radar cross-section of the sea surface 1. background model. *Journal of Geophysical Research: Oceans*, vol. 108, no. C3, pp. 1–24.

Kudryavtsev, V., Mastenbroek, C., and Makin, V. (1997). Modulation of wind ripples by long surface waves via the air flow: a feedback mechanism. *Boundary-Layer Meteorology*, vol. 83, pp. 99–116.

Kundu, P. K. and Cohen I. M. and Dowling, D. R (2016). *Fluid mechanics*. 6th ed. Elsevier.

Leppäranta, M. and Myrberg, K. (2009). *Physical Oceanography of the Baltic Sea*. 1st ed. Springer.

Leutbecher, M. et al. (2017). Stochastic representations of model uncertainties at ECMWF: state of the art and future vision. *Quarterly Journal of the Royal Meteorological Society*, vol. 143, no. 707, pp. 2315–2339.

Li, X. M. and Lehner, S. (2014). Algorithm for sea surface wind retrieval from TerraSAR-X and TanDEM-X data. *IEEE Transactions on Geoscience and Remote Sensing*, vol. 52, no. 5, pp. 2928–2938.

Lorenc, A. C. (1988). Optimal nonlinear objective analysis. *Quarterly Journal of the Royal Meteorological Society*, vol. 114, no. 479, pp. 205–240.

Lyzenga, D. R. and Marmorino, G. O. (1998). Measurement of surface currents using sequential synthetic aperture radar images of slick patterns near the edge of the gulf stream. *Journal of Geophysical Research: Oceans*, vol. 103, no. C9, pp. 18769–18777.

Madsen, S. N. (1989). Estimating the Doppler centroid of SAR data. *IEEE Transactions on Aerospace and Electronic Systems*, vol. 25(2), pp. 134–140.

Meyer, M. et al. (2018). Revisiting the estimate of the North Sea air-sea flux of CO2 in 2001/2002: the dominant role of different wind data products. *Journal of Geophysical Research: Biogeosciences*, vol. 123, no. 5, pp. 1511–1525.

Miles, J. W. (1957). On the generation of surface waves by shear flows. *Journal of fluid mechanics* , vol. 3, no. 2, 185–204.

Milliff, R. F. et al. (1999). Ocean general circulation model sensitivity to forcing from scatterometer winds. *Journal of Geophysical Research: Oceans*, vol. 104, no. C5, pp. 11337–11358.

Moreira, A. et al. (2011). “Tandem-L: A mission proposal for monitoring dynamic Earth processes”. *2011 IEEE International Geoscience and Remote Sensing Symposium*, pp. 1385–1388.

Moreira, A. et al. (2013). A tutorial on synthetic aperture radar. *IEEE Geoscience and Remote Sensing Magazine*, vol. 1, no. 1, pp. 6–43.

Mouche, A. et al. (2012). On the use of Doppler shift for sea surface wind retrieval from SAR. *IEEE Transactions on Geoscience and Remote Sensing*, vol. 50, no. 7, pp. 2901–2909.

Mouche, A. A., Hauser, D., and Kudryavtsev, V. (2006). Radar scattering of the ocean surface and sea-roughness properties: A combined analysis from dual-polarizations airborne radar observations and models in C-band. *Journal of Geophysical Research: Oceans*, vol. 111, no. C9.

Omstedt, A. et al. (2014). Progress in physical oceanography of the Baltic Sea during the 2003–2014 period. *Progress in Oceanography*, vol. 128, pp. 139 –171.

Ouchi, K. (1988). Synthetic aperture radar imagery of range traveling ocean waves. *IEEE Transactions on Geoscience and Remote Sensing*, vol. 26, no. 1, pp. 30–37.

Parard, G. et al. (2017). The potential of using remote sensing data to estimate air-sea CO2 exchange in the Baltic Sea. *Earth System Dynamics*, vol. 8, no. 4, pp. 1093–1106.

Philips, O. M. (1977). *The dynamics of the upper ocean*. 2nd ed. Cambridge University Press.

Phillips, O. M. (1957). On the generation of waves by turbulent wind. *Journal of Fluid Mechanics* , vol. 2, no. 5, 417–445.

Plant, W. J. (1990). Bragg scattering of electromagnetic waves from the air/sea interface. *Surface Waves and Fluxes: Volume II — Remote Sensing*. Ed. by G. L. Geernaert and W. J. Plant. Springer Netherlands.

Plant, W. J. and Keller, W. C. (1990). Evidence of Bragg scattering in microwave Doppler spectra of sea return. *Journal of Geophysical Research: Oceans*, vol. 95, no. C9, pp. 16299–16310.

Plant, W. J. (1986a). A two-scale model of short wind-generated waves and scatterometry. *Journal of Geophysical Research: Oceans*, vol. 91, no. C9, pp. 10735–10749.

Plant, W. J. (1986b). A two-scale model of short wind-generated waves and scatterometry. *Journal of Geophysical Research: Oceans*, vol. 91, no. C9, pp. 10735–10749.

Plant, W. J. (1997). A model for microwave Doppler sea return at high incidence angles: Bragg scattering from bound, tilted waves. *Journal of Geophysical Research: Oceans*, vol. 102, no. C9, pp. 21,131–21,146.

Plant, W. J. (2002). A stochastic, multiscale model of microwave backscatter from the ocean. *Journal of Geophysical Research: Oceans*, vol. 107, no. C9, pp. 3–1–3–21.

Plant, W. J. (2003). Microwave sea return at moderate to high incidence angles. *Waves in Random Media*, vol. 13, no. 4, pp. 339–354.

Raney, R. K. (1986). Doppler properties of radars in circular orbits. *International Journal of Remote Sensing*, vol. 7, no. 9, pp. 1153–1162.

Rascle, N. et al. (2008). A global wave parameter database for geophysical applications. part 1: wave-current–turbulence interaction parameters for the open ocean based on traditional parameterizations. *Ocean Modelling*, vol. 25, no. 3, pp. 154 –171.

Ren, Y. et al. (2012). An algorithm for the retrieval of sea surface wind fields using X-band TerraSAR-X data. *International Journal of Remote Sensing*, vol. 33, no. 23, pp. 7310–7336.

Richards, M. A. (2005). *Fundamentals of Radar Signal Processing*. Ed. by M. Richards. McGraw-Hill.

Richards, M. A., Scheer, J. A., and Holm, W. A. (2010). *Principles of Modern Radar: Basic Principles*. Ed. by M. A. Richards, J. A. Scheer, and W. A. Holm. SciTech Publishin.

Robinson, I. S. (2004). *Measuring the oceans from space*. 1st ed. Springer.

Rodgers, C. D. (2000). *Inverse methods for atmospheric sounding*. World Scientific.

Rodríguez, E. et al. (2019). The winds and currents mission concept. *Frontiers in Marine Science*, vol. 6, p. 438.

Röhrs, J. et al. (2015). Comparison of HF radar measurements with Eulerian and Lagrangian surface currents. *Ocean Dynamics*, vol. 65, no. 5, pp. 679–690.

Romeiser, R., Alpers, W., and Wismann, V. (1997). An improved composite surface model for the radar backscatter cross section of the ocean surface, 1. theory of the model and optimization / validation by scatterometer data. *Journal of Geophysical Research* , vol. 102, no. C11, pp. 25237–25250.

Romeiser, R. and Thompson, D. R. (2000). Numerical study on the along-track interferometric radar imaging mechanism of oceanic surface currents. *IEEE Transactions on Geoscience and Remote Sensing. Vol. 38-II, 446-458, 2000.*, vol. 38, no. 2, pp. 446–458.

Romeiser, R. et al. (Feb. 2010). Direct surface current field imaging from space by along-track InSAR and conventional SAR. *Oceanography from Space, Revisited*. Ed. by V. Barale, J. F. R. Grower, and L. Alberotanza. Springer. Chap. 5, pp. 73–91.

Rosen, P. A. et al. (2000). Synthetic aperture radar interferometry. *Proceedings of the IEEE*, vol. 88, no. 3, pp. 333–382.

Schiller, A. and Brassington, G. B. (2011). *Operational oceanography in the 21st century*. Ed. by A. Schiller and G. B. Brassington. Springer.

Schulz-Stellenfleth, J., König, T., and Lehner, S. (2007). An empirical approach for the retrieval of integral ocean wave parameters from synthetic aperture radar data. *Journal of Geophysical Research: Oceans*, vol. 112, no. C3.

Sebille, E. van et al. (2020). The physical oceanography of the transport of floating marine debris. *Environmental Research Letters*, vol. 15, no. 2, pp. 1–32.

Skolnik, M. I. (1970). *Radar handbook*. New York, NY: McGraw-Hill.

Smith, M. J., Poulter, E. M., and McGregor, J. A. (1996). Doppler radar measurements of wave groups and breaking waves. *Journal of Geophysical Research: Oceans*, vol. 101, no. C6, pp. 14269–14282.

Stoffelen, A. (2008). Scatterometer applications in the European seas. *Remote sensing of the European seas*. Ed. by V. Barale and M. Gade. Dordrecht: Springer Netherlands, pp. 269–282.

Stoffelen, A. and Anderson, D. (1993). Wind retrieval and ERS-1 scatterometer radar backscatter measurements. *Advances in Space Research*, vol. 13, no. 5, pp. 53 –60.

Stoffelen, A. (1998). Toward the true near-surface wind speed: error modeling and calibration using triple collocation. *Journal of Geophysical Research: Oceans*, vol. 103, no. C4, pp. 7755–7766.

Stokes, G. (1847). On the theory of oscillatory waves. *Transactions of the Cambridge Philosophical Society*, vol. 8, no. 441, pp. 197–229.

Thompson, D. R. (1989). Calculation of microwave Doppler spectra from the ocean surface with a time-dependent composite model. *Radar scattering from modulated wind waves*. Ed. by G. J. Komen and W. A. Oost. Dordrecht: Springer Netherlands, pp. 27–40.

Thompson, D. R. and Jensen, J. R. (1993). Synthetic aperture radar interferometry applied to ship generated internal waves in the 1989 Loch Linnhe experiment. *Journal of Geophysical Research: Oceans*, vol. 98, no. C6, pp. 10259–10269.

Tucker, M. J. (1985). The decorrelation time of microwave radar echoes from the sea surface. *International Journal of Remote Sensing*, vol. 6, no. 7, pp. 1075–1089.

Uihlein, A. and Magagna, D. (2016). Wave and tidal current energy – a review of the current state of research beyond technology. *Renewable and Sustainable Energy Reviews*, vol. 58, pp. 1070 –1081.

Ulaby, F. T. and Long, D. G. (2014). *Microwave radar and radiometric remote sensing*. 1st ed. The University of Michigan press.

Ulaby, F. T., Moore, R. K., and Fung, A. K. (1986). *Microwave remote sensing: active and passive, volume ii: radar remote sensing and surface scattering and emission theory*. 1st ed. Artech House.

Valenzuela, G. R. (1968). Scattering of electromagnetic waves from a tilted slightly rough surface. *Radio Science*, vol. 3, no. 11, pp. 1057–1066.

Valenzuela, G. R. (1978). Theories for the interaction of electromagnetic and oceanic waves — a review. *Boundary-Layer Meteorology*, vol. 13, no. 1, pp. 61–85.

Vesecky, J. F. and Stewart, R. H. (1982). The observation of ocean surface phenomena using imagery from the SEASAT synthetic aperture radar: an assessment. *Journal of Geophysical Research: Oceans*, vol. 87, no. C5, pp. 3397–3430.

Villas Bôas, A. B. et al. (2019). Integrated observations of global surface winds, currents, and waves: requirements and challenges for the next decade. *Frontiers in Marine Science*, vol. 6, p. 425.

Voronovich, A. (1994). Small-slope approximation for electromagnetic wave scattering at a rough interface of two dielectric half-spaces. *Waves in Random Media*, vol. 4, no. 3, pp. 337–367.

Wackerman, C. C. et al. (1996). Wind vector retrieval using ERS-1 synthetic aperture radar imagery. *IEEE Transactions on Geoscience and Remote Sensing*, vol. 34, no. 6, pp. 1342–1352.

Witter, D. L. and Chelton, D. B. (1991). A Geosat altimeter wind speed algorithm and a method for altimeter wind speed algorithm development. *Journal of Geophysical Research: Oceans*, vol. 96, no. C5, pp. 8853–8860.

Wong, F. H. and Cumming, I. G. (1996). A combined SAR Doppler centroid estimation scheme based upon signal phase. *IEEE Transactions on Geoscience and Remote Sensing*, vol. 34, no. 3, pp. 696–707.

Wright, J. (1966). Backscattering from capillary waves with application to sea clutter. *IEEE Transactions on Antennas and Propagation*, vol. 14, no. 6, pp. 749–754.

Wright, J. (1968). A new model for sea clutter. *IEEE Transactions on Antennas and Propagation*, vol. 16, no. 2, pp. 217–223.

Wu, J. (1983). Sea-surface drift currents induced by wind and waves. *Journal of Physical Oceanography*, vol. 13, no. 8, pp. 1441–1451.

Wu, Y., Zhai, X., and Wang, Z. (Nov. 2017). Decadal-mean impact of including ocean surface currents in bulk formulas on surface air–sea fluxes and ocean general circulation. *Journal of Climate*, vol. 30, no. 23, pp. 9511–9525.

Young, I. R., Rosenthal, W., and Ziemer, F. (1985). A three-dimensional analysis of marine radar images for the determination of ocean wave directionality and surface currents. *Journal of Geophysical Research: Oceans*, vol. 90, no. C1, pp. 1049–1059.